The effect of contact areas on seepage behavior in 3D rough fractures under normal stress

Man Li
Chongqing University
Xianshan Liu (liuxianshan@163.com)
Chongqing University https://orcid.org/0000-0001-6021-9475
Yu Li
Chongqing University
Zelin Hou
Chongqing University
Shihao Qiao
Chongqing University

Research Article

Keywords: Rough fracture, Non-linear seepage, Contact ratio, Critical Reynolds number

Posted Date: March 30th, 2021

DOI: https://doi.org/10.21203/rs.3.rs-322946/v1

Version of Record: A version of this preprint was published at International Journal of Geomechanics on April 1st, 2022. See the published version at https://doi.org/10.1061/(ASCE)GM.1943-5622.0002330.

The effect of contact areas on seepage behavior in 3D rough fractures under normal stress

Man Li [1,2], Xianshan Liu [1,2,*], Yu Li [1,2], Zelin Hou[1,2], Shihao Qiao[1,2]

[1]*School of Civil Engineering, Chongqing University, Chongqing,400045, China*

[2]*National Joint Engineering Research Center of Geohazards Prevention in the Reservoir Areas, Chongqing 400045, China*

Abstract

The investigation of fluid flow in fractured rocks is a key issue in underground engineering. Reservoir sandstones as a case study, three specimens with different roughness using the Brazilian splitting were scanned to get the geometric morphology and aperture distribution, and the fractal dimension was introduced to characterize the fracture roughness. The flow experiments through the rough fractures subjected to different normal stresses were conducted to analyze the influence of the fractal dimension and the contact ratio on the nonlinear flow behavior, proving that the Forchheimer equation could better describe the flow nonlinearity. A modified Bandis model based on the experiments was proposed to calculate the max normal displacement of fracture under different normal stresses. Besides, a new model to forecast the nonlinear coefficient B was developed depending on the fractal dimension and the contact ratio, and a semi-empirical equation was employed to describe the critical Reynolds number. The influence of contact on the seepage path is simulated by COMSOL.

Keywords: Rough fracture, Non-linear seepage, Contact ratio, Critical Reynolds number

*Corresponding author at: School of Civil Engineering, Chongqing University, Chongqing,400045, China.
E-mail address: **liuxianshan@163.com** (X. Liu).

1 Introduction

The research on the seepage characteristics and solute transport processes in fractured rock masses have always been a hot topic in the field of underground engineerings, such as the extraction of shale and unconventional natural gas, the geological storage of CO_2, the development of geothermal energy, and the disposal of nuclear waste (Babadagli et al. 2015; Chen et al. 2014; Ranjith and Darlington 2007; Rutqvist 2015; Yu et al. 2020; Zou et al. 2017). The permeability of the rock matrix is extremely low, and the seepage channels in fractured rock masses are mainly composed of fracture networks, however, due to the complexity of the fracture network, single fracture seepage as the basic unit of fracture network should be the focus of research. The Navier-Stokes equation can better describe the characteristics of single-fracture seepage, however, owing to the complexity of solving the convection term, it takes a lot of calculation costs. Thus, the Navier-Stokes equation is generally simplified to the classic cubic law (Brush and Thomson 2003; Wang et al. 2015; Zimmerman and Yeo 2000). In the low-speed smooth parallel-plate model, the cubic law can indeed characterize the seepage characteristics of fractures well, but natural fractures are usually rough and undulating, and the actual engineering is at a state of high water pressure. At this time, the seepage behavior has transformed into nonlinearity, and the use of the cube law tends to overestimate the flow of the fracture (Brown 1987; Zhang et al. 2019; Zimmerman et al. 2004). Therefore, (Chen et al. 2015; Chen et al. 2019; Javadi et al. 2010; Zhang and Nemcik 2013) many researchers introduced the Forchheimer equation to characterize the nonlinear seepage behavior of rough fractures under high Reynolds numbers.

Due to the influence of the stress environment in the naturally fractured rock mass, the rough fractures are generally not in a completely mated state. Under the action of stress, the rough fracture channels undergo contact closure, shear dilatation, and other phenomena, resulting in the heterogeneity of the distribution of the fracture channels, which in turn affect the seepage characteristics of rough fractures. (Crandall et al. 2010; Javadi et al. 2014; Rong et al. 2016; Song et al. 2019; Zhou et al. 2015) A large number of experiments and numerical simulations have found that contact in rough fracture has a great impact on seepage behavior. Li et al. (2008) conducted several parallel-plate model hydraulic experiments under different contact ratios and found that the larger the contact ratio, the more experimental values of the hydraulic conductivity deviated from

the cubic model. Xia et al. (2017) found that the contact of the coarse fracture surface and the high Reynolds number led to the nonlinear seepage flow through the experimental method. Chen et al. (2017) launched seepage experiments under different normal stresses and compared with the Yeo (2001) model, establishing a three-parameter model of fracture permeability, hydraulic aperture, fractal dimension, and contact ratio. Xiong et al. (2018b) observed through the seepage experiment and numerical simulation under different normal stresses that contact of the rough fracture made the seepage path tortuous, and the tortuosity increased with the rise of the contact ratio, resulting in eddy and backflow, which eventually influenced the nonlinearity of seepage behavior. Although many studies have been carried out on the effect of fracture contact on seepage flow, there are few investigations on seepage characteristics of contact non-uniform distribution under stress in rough fractures. Therefore, it is necessary to further study it. This paper aims to improve the understanding of the influence of the contact on seepage under normal stress in single rough fractures.

The normal stress has a significant effect on the seepage characteristics in rock fractures because it can deform and close the asperities of the fractures, which will greatly change the geometry of the fracture. When subjected to normal stress, due to the uneven distribution of rough fracture apertures and the uncertainty of the constitutive relationship between normal stress and normal displacement, the determination of the contact under certain stress in rough fracture has always been one of the difficulties in the field of fractured rock mass seepage. Therefore, (Bandis et al. 1983; Greenwood and Williamson 1966; Pyraknolte and Morris 2000; Zhao et al. 2020; Zou et al. 2019) many investigations have been conducted on the constitutive relationship between normal stress and normal displacement of fractures, among which the hyperbolic model proposed by Bandis et al. (1983) is widely used. However, the actual rough fracture cannot be completely closed, so it is not accurate to calculate the contact with the initial average aperture of fracture instead of the maximum compression displacement (Li et al. 2015; Xiong et al. 2018a), which will ultimately affect the seepage of the rough fracture.

In the present study, we conducted a large number of high-precision hydraulic experiments on three different rough fractured sandstone samples at normal stress in the range of 1-30MPa. The nonlinear flow characteristics of the fluid were analyzed and the reasons for the nonlinear flow were discussed. The innovations of this work are as follows: (1) A modified Bandis model considering the roughness of the fracture was

proposed to calculate the normal closure displacement under normal stress. (2) Based on the results of hydraulic experiments, a model was established to characterize the nonlinear coefficient B in the Forchheimer equation with the contact ratio and fractal dimension of fracture, and a semi-empirical formula for the critical Reynolds number was derived. (3) The fluid flow process under different normal stresses was simulated, and the streamline distribution was used to directly clarify the influence of the contact of fracture on the seepage path, resulting in the nonlinearity of seepage.

2 Experimental methodology

2.1 Physical and mechanical properties of the selected rocks

The sandstones taken from Jiulongpo in Chongqing were selected for the experimental study (Fig. 1(a)), and the X-Ray Diffraction (XRD) testing indicated that quartz and feldspar (Anorthite) were mainly inside the sandstones. According to the method by the International Society for Rock Mechanics (ISRM), the size of all tested sandstone specimens shown in Fig. 1(b) is cylindrical with 50mm in diameter and 100mm in length approximately. Furthermore, three specimens were chosen to conduct mechanical tests and get the uniaxial compressive strength (UCS), Young's modulus, Poisson's ratio, porosity, and density listed in Table 1. The minor difference of the mechanical parameters for three specimens illuminates that these sandstone specimens are uniform to avoid the rock heterogeneity influencing the experimental efficiency and accuracy, which is crucial for deep research on the flow behavior of the rock fractures subjected to different normal stresses.

Table 1 Physico-mechanical properties of the sandstones

Specimens	UCS (MPa)	Young's modulus (GPa)	Poisson's ratio	Porosity (%)	Density (kg/m^3)
T1	56.46	10.28	0.22	8.57	2396.97
T2	56.18	9.94	0.27	8.58	2417.56
T3	55.25	10.08	0.26	8.62	2401.73
Mean	55.96	10.10	0.25	8.59	2405.42

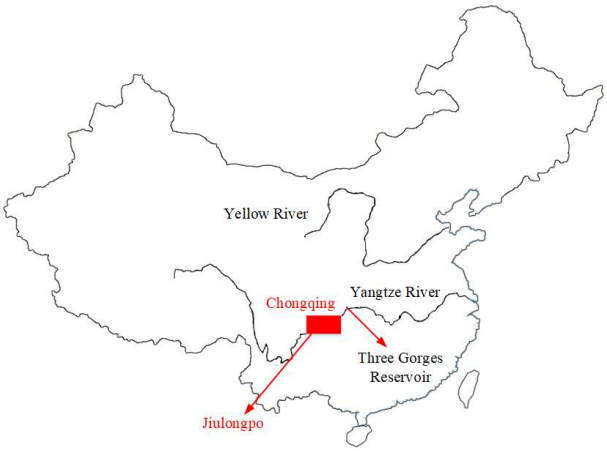

(a) Sampling location: Jiulongpo

(b) Sandstones specimens

Fig. 1 Specimens of sandstone

2.2 Preparation and measurement of rock rough fractures

To obtain the artificial rough tensile fractures with different morphology, some prepared sandstone specimens (Fig. 2(a)) were split using the Brazilian splitting test into two halves (Yang et al. 2015; Zhou et al. 2015). In the process of this splitting test, the significant difference of fractures morphology are presented when conducting different loading rate, it can be observed from these split upper and lower fractures that greater loading rate causes smaller asperity, otherwise, greater roughness will generate, as shown in Fig. 2(b).

Besides, three representative fractures with different roughness were selected and marked as S1, S2, and S3, then these fractures were scanned by the laser scanning system to get the geometric morphology. The advanced 3-Dimensional non-contact optical scanner called OKIO-B was applied to map the fracture geometry. The device offers the advantages of high precision, favorable repeatability, and exhibits real-time photographs to get the point cloud data of the 3-Dimensional rough fractures surface. The scanning space is 1mm, and the resolution of a sampling point obtained by the scanning system is ± 20 μm. Furthermore, the points cloud data based on the scanning system were optimized by noise reduction and patching treatment, and then imported

to the software MATLAB to reconstruct the 3-Dimensional fracture surface plotted in Fig. 3. Moreover, the above points cloud data was changed into Cartesian Coordinates and treated by a self-coded Matlab program to analyze the fracture aperture, the detailed calculation process was as follows (Liu et al. 2020b; Wanniarachchi et al. 2018).

Also, the initial aperture distribution of fracture S1, S2, and S3 is obtained and presented in Fig.4. The initial aperture of rough fractures presented a Gaussian distribution and the fitting correlation coefficient is greater than 0.978. Moreover, the corresponding mean value (e_m) and standard deviation (σ_f) of the fractures aperture can be expressed as $e_m = \frac{1}{m \times n} \sum_{i=1}^{m} \sum_{j=1}^{n} e_{ij}$, $\sigma_f = \sqrt{\frac{1}{m \times n - 1} \sum_{i=1}^{m} \sum_{j=1}^{m} (e_{ij} - e_m)^2}$ .The detailed values are listed in Table 2.

(a)Brazilian test

(b) Fracture surface after the Brazilian testing

Fig. 2 Sandstone rough fracture preparation

Table 2 Parameters of rough fracture surface S1-S3

Specimens	Length (mm)	Width (mm)	*JRC*	Aperture		Fractal parameters	
				Mean (e_m mm)	**Standard deviation (σ_f)**	D_v	K_v
S1	99.84	49.96	16.33	0.251	0.060	1.442	0.0498
S2	100.52	50.92	15.65	0.401	0.103	1.427	0.0286
S3	100.06	50.21	15.33	0.458	0.101	1.408	0.0337

2.3 Characterization of rough fractures

(Ge et al. 2014; Rong et al. 2016; Xiong et al. 2018b) Many studies indicated that the morphology of natural fracture was self-affine rather than self-similar, Kulatilake et al. (2007) supposed the fractures as self-affine profiles and proposed a variogram method to evaluate corresponding fractal dimension. The detailed expression is written by formula (1), representing the roughness of the fracture surface.

$$2\gamma(x,l)=\frac{1}{N}\sum_{i=1}^{N}\left[Z(x_i+l)-Z(x_i)\right]^2 \qquad (1)$$

where $\gamma(x,l)$ is the semi-variogram, $Z(x_i+l)$ and $Z(x_i)$ are the heights of the profile from the baseline, l is the space of the adjacent points from the baseline, N is the number of points in the baseline. When considering $l\to 0$, $\gamma(x,l)$ can be simplified as a power-law function (Eq. (2)) for the self-affine model.

$$2\gamma(x,l)=K_v l^{2H} \qquad (2)$$

where K_v is a proportionality constant, H is the Hurst exponent, (Liu et al. 2020a; Wang et al. 2016) demonstrating that greater H represents smoother fracture surface, which is related to the fractal dimension D_v ($D_v=2-H$). However, the fractal dimension D_v cannot be calculated using Eqs. (1) and (2) directly, thus the logarithmic expressions should be used to solve D_v.

$$\log(2\gamma(x,l))=\log K_v+2(2-D_v)\log l \qquad (3)$$

And then, 11 sectional profiles parallel to the flow direction at intervals of 5 mm were extracted to obtain the fractal dimension D_v and constant K_v based on the proposed variogram method. Firstly, (Tse and Cruden 1979) the joint roughness coefficient (JRC) of the selected specimens as the significant coefficient to describe fracture morphology was calculated with the formula (4-5) and listed in Table 2. Secondly, according to Kulatilake et al. (Ge et al. 2014; Kulatilake et al. 2007) studies, choosing nine values to calculate $\gamma(x,l)$ using an increment factor of 1.2 starting from 2. The relationship between the variogram $2\gamma(x,l)$ and space l shown in Figure. 5 is better fitted by the logarithmic function with the correlation coefficient valued $R^2>0.943$. It can be concluded from Table 2 that the fractal dimension D_v varied in the range of 1.408 and 1.442, and D_v is greater for rougher fractures surface, which is in good agreement with the change of the JRC.

$$Z_2=\left[\frac{1}{(n-1)(\Delta x)^2}\sum_{i=1}^{n}\left(Z_{i+1}-Z_i\right)^2\right]^{\frac{1}{2}} \qquad (4)$$

$$\mathrm{JRC}=32.2+32.47\log Z_2 \qquad (5)$$

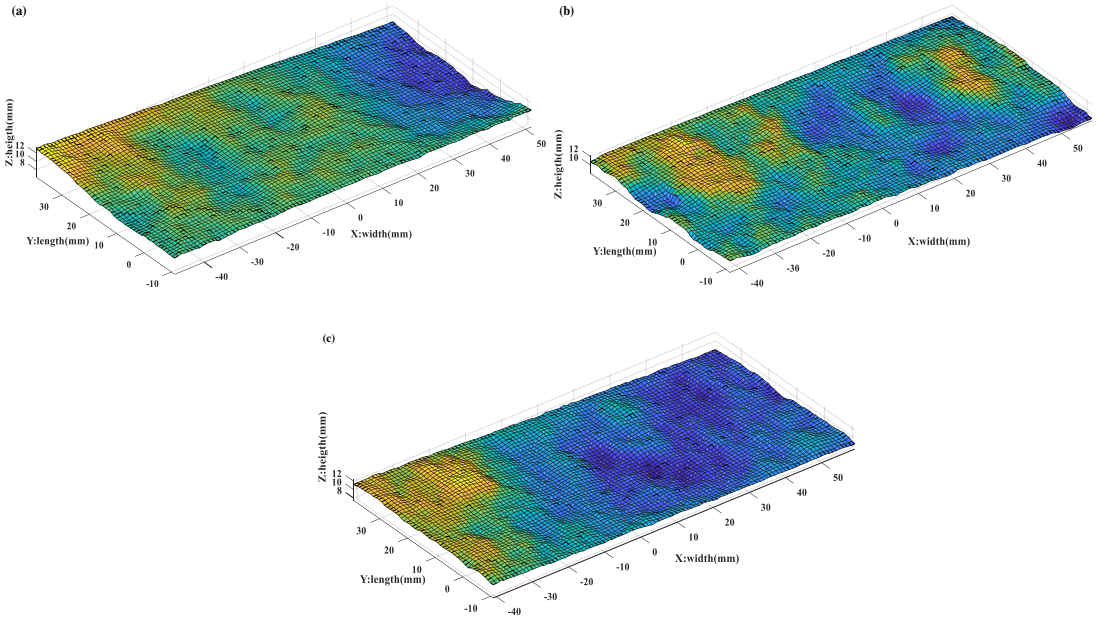

185

186

187 **Fig. 3** 3-Dimensional morphology reconstruction of rough fracture of specimens:(a)-(c)

188 specimens

189

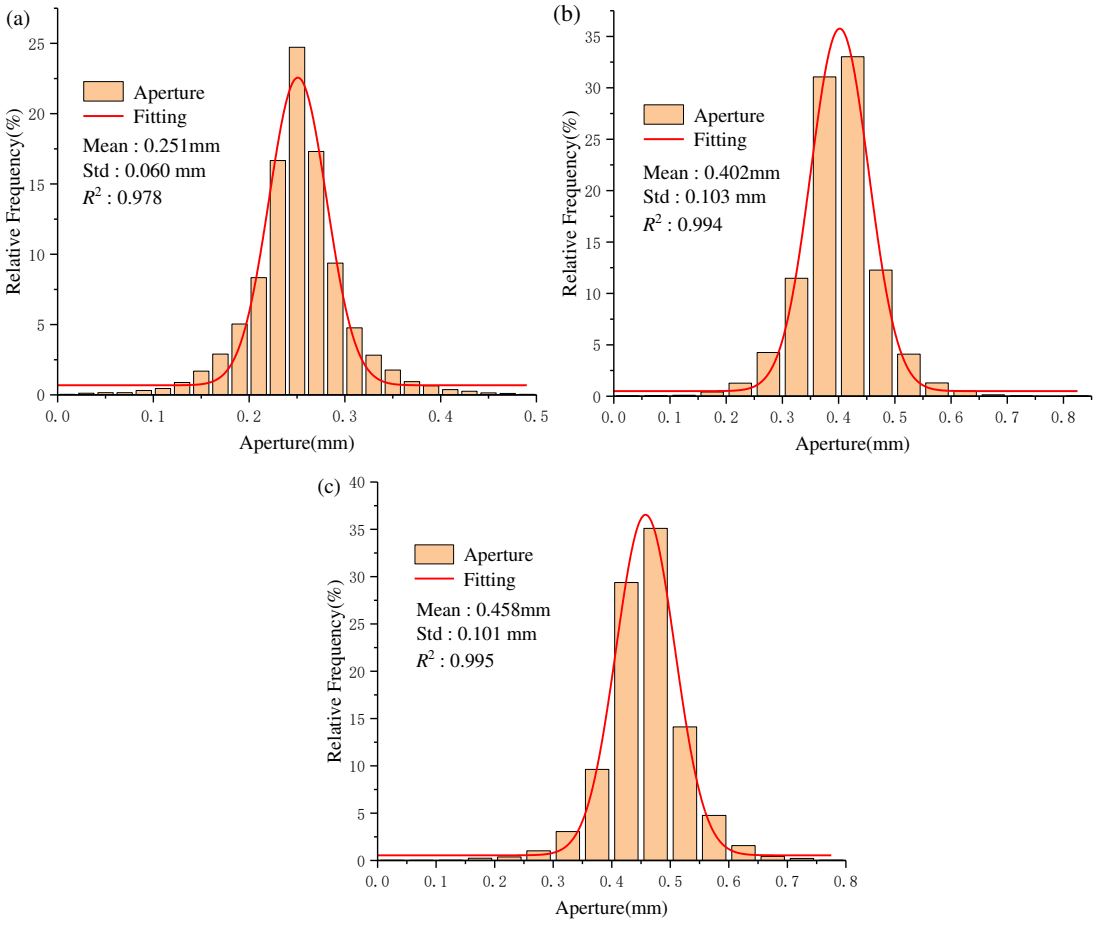

190

191

192 **Fig. 4** Aperture distribution of rough fracture surface : (a)-(c) specimens S1-S3

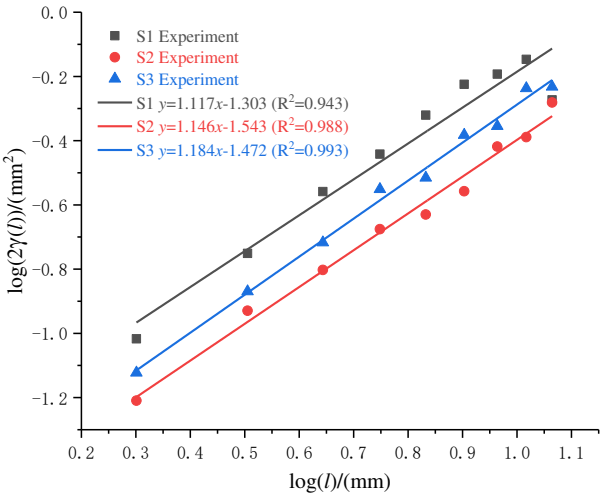

Fig. 5 Fitting curves of the $\log(2\gamma(l))$ and $\log(l)$ in rough fracture surface S1-S3

2.4 Testing procedure

All tests were carried out on a rock servo-controlled triaxial equipment called Rock 600-50HT PLUS manufactured by TOP-INDUSTRIE in France plotted in Fig. 6. The triaxial cell is capable of performing triaxial compression tests at confining pressures (P2) up to 60 MPa, with increasing deviatoric stress (P1) up to 500 MPa, with increasing transducer has a resolution of 0.01MPa. The system can deal with the constant-head, constant flow-rate, and transient-pulse permeability tests under low or high confining and water pressures, and a high precision electronic balance is selected to measure the real-time flow rate (Liu et al. 2020c). The servo-controlled fluid pump can produce pore pressure up to 60MPa (P3/P4). Furthermore, the upstream and downstream fluid pressure can be regulated with pore pressure pump P3 and P4, as a result, the seepage tests can be performed on constant fluid pressure or constant volume condition according to the experimental target.

As for the flow procedure, the sandstone specimens are firstly saturated, then vacuumed for 4 hours by the vacuum pump and wet pumped for 4 hours with distilled water, finally soaked for 16 hours to ensure the specimens full of water. And then, the specimens are enclosed in a 3-mm-thick Viton rubber jacket and then placed in the sample assembly. Porous spacers are inserted onto the ends of the samples to ensure even distribution of pore pressure over the ends of the samples. Considering the influence of the temperature on deformation and seepage response, all the tests are performed at room temperature (25±2°C). The seepage tests under different load combinations can be performed as follows. The samples are firstly applied with the confining pressure of the desired value, and at this stage the axial stress is proportionally

increased to the value of the confining pressure, bringing the samples to initial isotropic stress or zero deviatoric stress to ensure that there is no gap between the specimen and the rubber jacket to prevent the fluid leakage. Furthermore, the saturated specimens are conducted at a constant pore pressure indicating the balance of the upstream pressure (P3) and downstream pressure (P4) to ensure the fluid in a single phase in the process of seepage testing. Afterward, water is introduced into the fractures through the inlet and collected at the outlet. A series of flow pressures at the inlet were tested and their corresponding flowrates were recorded. Therefore, the relationships between flowrate and pressure gradient or hydraulic gradient for the rough fractures can be obtained under different confining stresses.

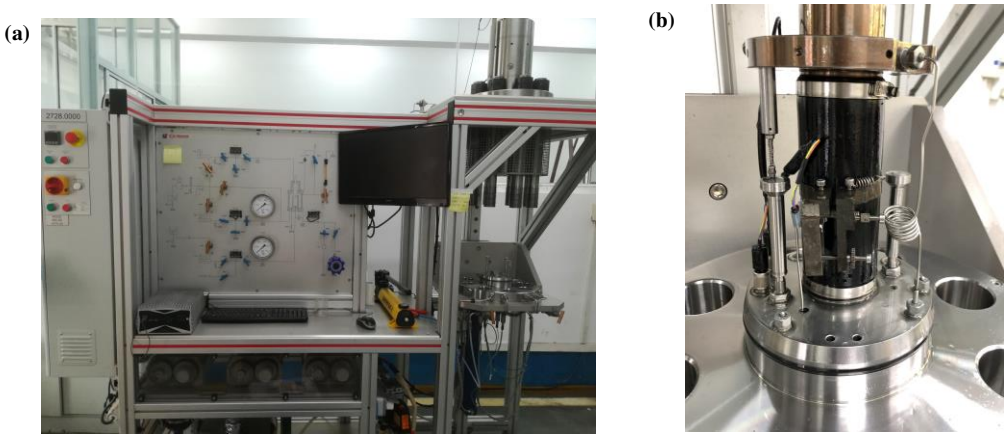

Fig. 6 Triaxial multi-field coupling test system

3 Experimental results and discussion

3.1 Normal stress-induced fracture closure

The normal compression displacement of the fractured rock sample under confining pressure can be measured in real-time with a hoop strain gauge，and the relationship curve between the normal compression displacement and normal stress of the sandstone specimens S1-S3 is shown in Fig 7. (Bandis et al. 1983; Li et al. 2015) Many investigations have demonstrated the hyperbola relationship between the normal closure displacement Δu and normal stress σ_n , the so-called classic Bandis model as follows.

$$\sigma_n = k_{n0}\left(\frac{\Delta u}{1-\Delta u / u_{max}}\right) \qquad (6)$$

where k_{n0} is the normal stiffness of the fracture, $u_{\max}$ is the maximum compression displacement. The normal stress and normal displacement are fitted according to the Bandis model. It can be seen from Fig 7 that the relationship between normal stress and the normal displacement of the sample S1-S3 has a good correlation ($R^2 > 0.928$), and the fitted correlation coefficient is shown in Table 3. The maximum compression displacement $u_{\max}$ for specimens S1, S2, and S3 is then calculated as 0.242mm, 0.388mm, and 0.447mm using the regression method, which is 96.25%、96.73%、97.55% of the initial mean apertures (e_m). Overall, the results demonstrated that the surface is rougher, and the ratio of the maximum compression displacement and the initial mean aperture ($u_{\max} / e_m$) is smaller. This is because the greater the roughness of the fracture surface, the greater the number of contact pairs between the upper and lower fracture surfaces, causing resistive deformation in the axial direction, which is manifested in the fact that the normal stiffness decreases as the fractal dimension decreases.

Many studies have shown that the contact of fracture under stress will have a greater impact on seepage behavior, so it is necessary to calculate the contact ratio under stress. From formula (6), the closure displacement under specific stress can be calculated, as in formula (7):

$$\Delta u = \frac{\sigma_n u_{max}}{k_{n0} u_{max} + \sigma_n} \qquad (7)$$

Due to the undulations of the fracture surface geometry, the maximum compression displacement is difficult to accurately calculate. In previous studies, the initial average aperture is often used instead, which is not suitable. Based on the experimental results, this paper proposes a modified formula considering the fractal dimension of the fracture to characterize the maximum compression displacement of the fracture as follows:

$$u_{max} = \lambda \frac{e_m}{D_v} \qquad (8)$$

λ is the dimensionless coefficient, which is obtained by the least square method, and the correlation coefficient is greater than 0.999. Substituting formula (8) into formula (7) can derive the modified Bandis model:

$$\Delta u = \frac{\lambda e_m \sigma_n}{\lambda e_m k_{n0} + D_v \sigma_n} \qquad (9)$$

The initial fracture aperture distribution (e_{ij}) at each position of the fracture surface can be obtained from (Liu et al. 2020b). When normal stress is applied, the fracture will have a compression displacement, and the fracture aperture becomes $e_{ij}^{'}$, as shown in formula (10). Once the fracture aperture $e_{ij}^{'}$ is negative, it can be concluded that the normal deformation is so large to result in the contact of the upper surface and the lower surface. However, zero aperture is not common for real fractures, so a small value called residual aperture e_r ($e_r = 10^{-6}$ m) is supposed to all the contact elements considering good precision of current testing apparatus and solution singularity of numerical simulations.

$$e_{ij}^{'} = \begin{cases} Z_{Tij} - Z_{Bij} + \Delta u & \text{if } Z_{Tij} + \Delta u > Z_{Bij} \\ e_r & \text{if } Z_{Tij} + \Delta u \le Z_{Bij} \end{cases} \qquad (10)$$

The calculation formula of the contact ratio can be written:

$$c = \frac{N_c}{N_T} \qquad (11)$$

where c is the contact ratio, N_c is the number of the contact elements of the rough fracture, N_T is the total elements of the rough fracture.

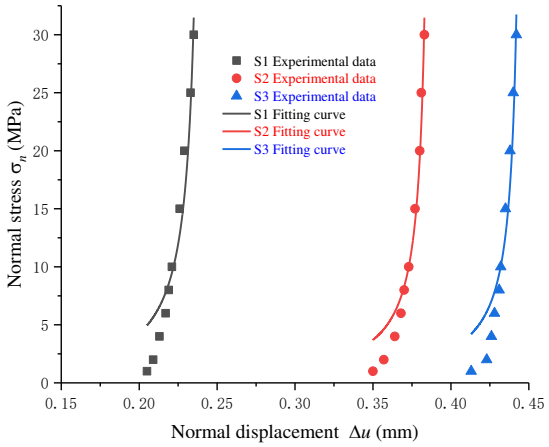

Fig.7 Relationship curve between normal stress and normal displacement

289 **Table 3** Fitting parameters based on the Bandis model

Specimens	k_{n0} (GPa/m)	u_{max} (mm)	R^2
S1	3.653	0.242	0.930
S2	1.032	0.388	0.964
S3	0.772	0.447	0.928

290 ## 3.2 Nonlinear characteristics of the seepage

291 The testing data under different normal stresses have been obtained precisely, and
292 curves of the pressure gradient ∇P and the flow rate Q at the outlet for specimens
293 S1-S3 were plotted in Fig. 8. As observed from Fig.8, the flow behavior through the
294 rough fractures changed obviously. It can be concluded that fluid flow mainly presents
295 darcy flow behavior through rough fractures at a smaller pressure gradient. With the
296 increase of the pressure gradient, the friction effect of the rough fracture surface is
297 significant, and the fluid inertial force becomes not negligible, showing a gradual
298 transformation from linear to nonlinear flow regime in the rough fractures. Hence, the
299 parallel plate model (cubic law) can't accurately describe the nonlinear behavior. With
300 the rise of normal stress, the contact areas of the upper fracture surface and lower
301 fracture surface gradually increase, resulting in a great decline of the flow rate and
302 obvious tortuosity of the flowing channels. For quantitatively presenting the nonlinear
303 behavior through the rough fractures caused by the flow inertial forces, the widely used
304 Forchheimer model was adopted, as follows (Chen et al. 2015; Liu et al. 2016).

305 $$-\nabla P = AQ + BQ^2 \qquad (12)$$

306 $$A = \frac{12\mu}{we_h^3} \qquad (13)$$

307 $$B = \frac{\beta\rho}{w^2 e_h^2} \qquad (14)$$

308 where AQ is the linear term by viscous forces, BQ^2 is the nonlinear term by
309 inertial forces, ∇P is the pressure gradient, Q is the flowrate through the fractures,
310 A and B represent the linear coefficients and nonlinear coefficients, respectively,
311 ρ is the fluid density, w is the fracture width, β is the non-Darcy coefficient, μ
312 is the dynamic viscosity of the fluid, e_h is the equivalent hydraulic aperture.

The Forchheimer model is introduced to conduct regressive analysis for corresponding testing data of ∇P and Q under different normal stresses, and the fitting curves are shown in Fig. 8 and the detailed fitting coefficients are listed in Table 4. The regressive expressions with a correlation coefficient greater than 0.993 indicated that the Forchheimer model can better characterize the nonlinear flow caused by the inertial forces under a greater pressure gradient. The variation of the linear coefficient A and the nonlinear coefficient B is presented in Fig. 9, respectively. It is noted that both coefficients show an upward trend with increasing confining pressure, resulting in larger contacts in the fractures, and an abrupt drop of equivalent hydraulic aperture (Fig. 10). Especially, the contact of the upper fracture surface and lower fracture surface weakening the effective flow channels can not be ignored when investigating the flow through the rough fractures, so the influence of contact on the transformation mechanism of seepage behavior in rough fractures should be thoroughly examined under different normal stresses.

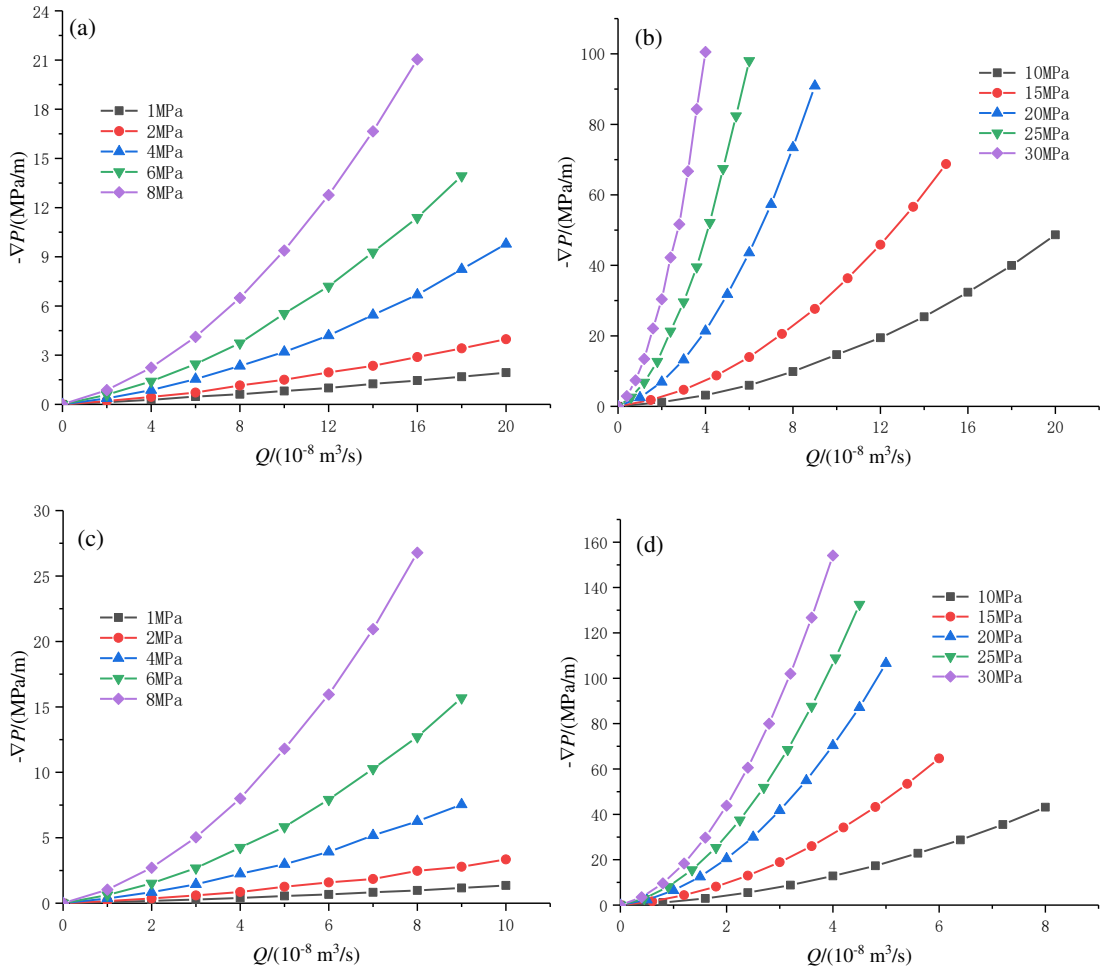

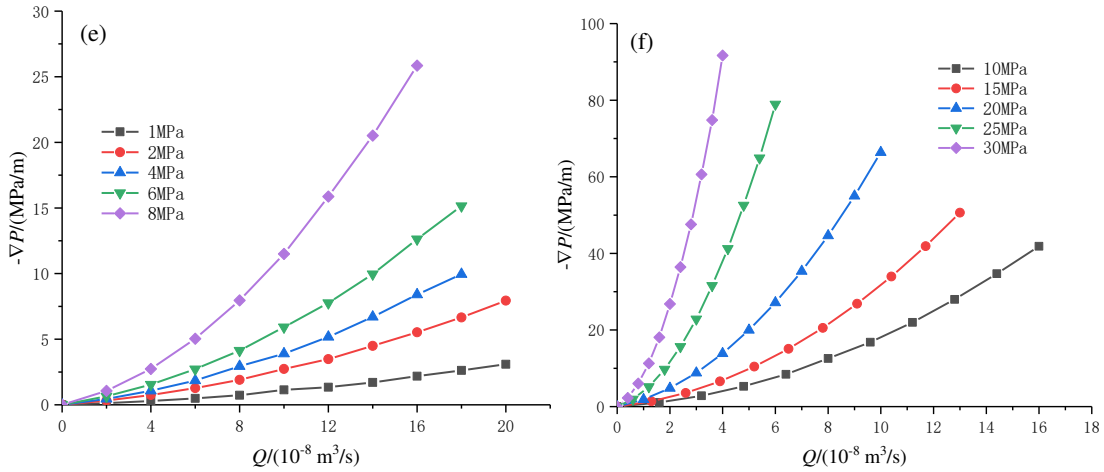

Fig. 8 Curves of $\nabla P - Q$ for specimens S1-S3 at different confining stresses:(a)S1 at 1-8MPa,(b)S1 at 10-30 MPa; (c)S2 at 1-8 MPa,(d)S2 at 10-30 MPa; (e)S1 at 1-8 MPa,(f)S1 at 10-30 MPa.

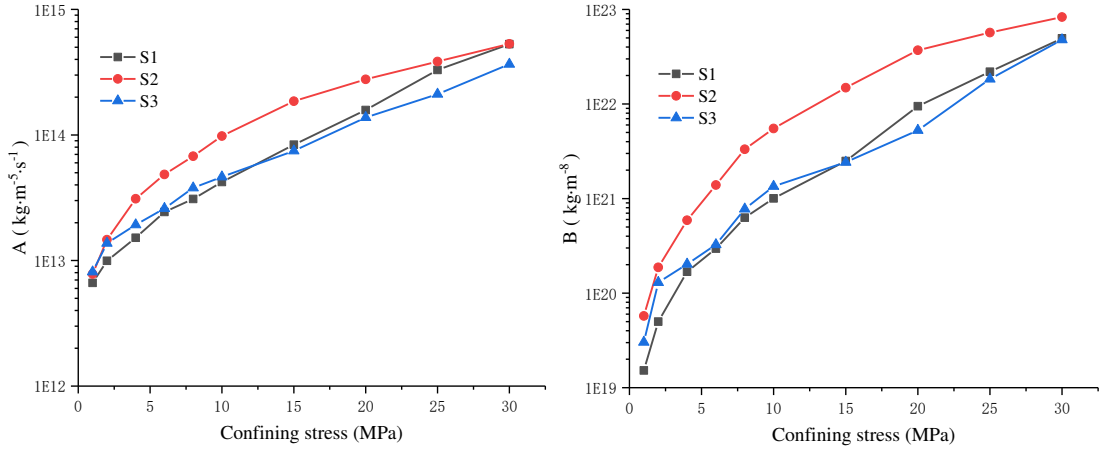

Fig. 9 Relationship curve Forchheimer equation coefficients and confining pressure for S1-S3:(a) Coefficient A , Coefficient B

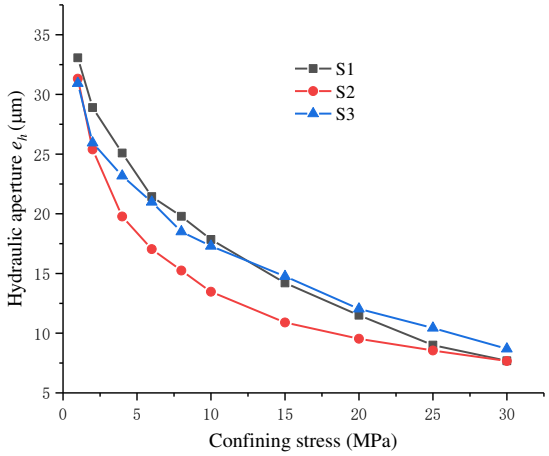

Fig. 10 Variation of the hydraulic aperture with confining stress

340 **Table 4** Fitting parameters of the Forchheimer equation for specimens S1-S3

Specimens	Confining stress(MPa)	$A(10^{12}\cdot kg\cdot m^{-5}\cdot s^{-1})$	$B\ (10^{19}\cdot kg\cdot m^{-8})$	Hydraulic aperture (μm)	R^2(-)
S1	1	6.64	1.52	33.070	0.999
	2	9.94	5.00	28.902	1.000
	4	15.19	16.85	25.092	0.997
	6	24.34	29.55	21.443	0.999
	8	30.94	62.84	19.795	1.000
	10	42.20	100.29	17.850	0.998
	15	83.71	249.34	14.206	0.999
	20	157.77	947.71	11.501	0.999
	25	329.38	2195.11	8.998	0.998
	30	528.99	4951.16	7.684	0.999
S2	1	7.81	5.74	31.322	1.000
	2	14.66	18.73	25.391	1.000
	4	31.06	58.99	19.769	0.999
	6	48.51	139.24	17.040	0.999
	8	67.72	332.51	15.247	0.996
	10	98.07	550.64	13.476	0.999
	15	185.68	1489.11	10.893	0.998
	20	277.21	3700.68	9.531	0.993
	25	384.05	5692.88	8.549	0.999
	30	531.48	8302.64	7.672	0.998
S3	1	8.11	3.03	30.929	0.999
	2	13.74	12.98	25.944	1.000
	4	19.27	20.28	23.180	0.997
	6	25.97	32.54	20.985	0.999
	8	37.86	77.56	18.507	0.999
	10	46.33	134.71	17.303	0.998
	15	74.62	242.26	14.761	1.000
	20	137.73	526.34	12.034	0.999
	25	211.23	1839.04	10.435	0.999
	30	366.18	4788.01	8.686	0.998

341 ## 3.3 The transformation of the flow behavior

342 It can be seen from the fitted curves of $\nabla P \sim Q$ that seepage characteristics in the
343 rough fractures will transform from linear to nonlinear, so the transformation
344 mechanism of the flow behavior should be further studied. Reynolds number Re
345 written by formula (15) is a key parameter to describe the ratio of the inertial forces and
346 the viscous forces, revealing that Re increases with the rise of flow velocity causing
347 greater inertial forces.

348 $$Re = \frac{\rho u e_h}{\mu} = \frac{\rho Q}{\mu w} \qquad (15)$$

349 where ρ , Q , w , e_h has been described in Eqs. (12)-(14), u is the average
350 velocity of the fracture.

351 To investigate the influence of nonlinear terms on percolation behavior based on
352 the Forchheimer equation, (Zeng and Grigg 2006; Zhou et al. 2015) the non-Darcy

353 effect factor E proposed by Zeng et al was introduced to explain the mechanism of
354 nonlinear seepage in the rough fractures, as follows.

355 $$E = \frac{BQ^2}{AQ + BQ^2} \qquad (16)$$

356 where E represents the strength of the flow nonlinearity. The inertial forces can't
357 be ignored when the parameter E reaches 10% in the geotechnical field, indicating
358 the nonlinear flow behavior has been triggered. Thus, the critical Reynolds number
359 Re_c based on formulas (12) and (13) can be derived as follows.

360 $$Re_c = \frac{A\rho E}{B\mu w(1-E)} \qquad (17)$$

361 The non-Darcy effect factor at different confining pressure can be calculated based
362 on Forchheimer coefficients A , B, and curves of $E \sim Q$ and $E \sim Re$ are plotted
363 in Fig.11. E increased with rising Reynolds number or flow rate, which can be used
364 to determine the critical Reynolds number when nonlinear flow occurred. The critical
365 Reynolds number Re_c of specimens S1, S2, and S3 subjected to normal stress
366 σ_n=1~10MPa is in the range of 0.08~0.97, showing a good agreement with the results
367 in Brush et al (Brush and Thomson 2003; Radilla et al. 2013; Zhou et al. 2016).

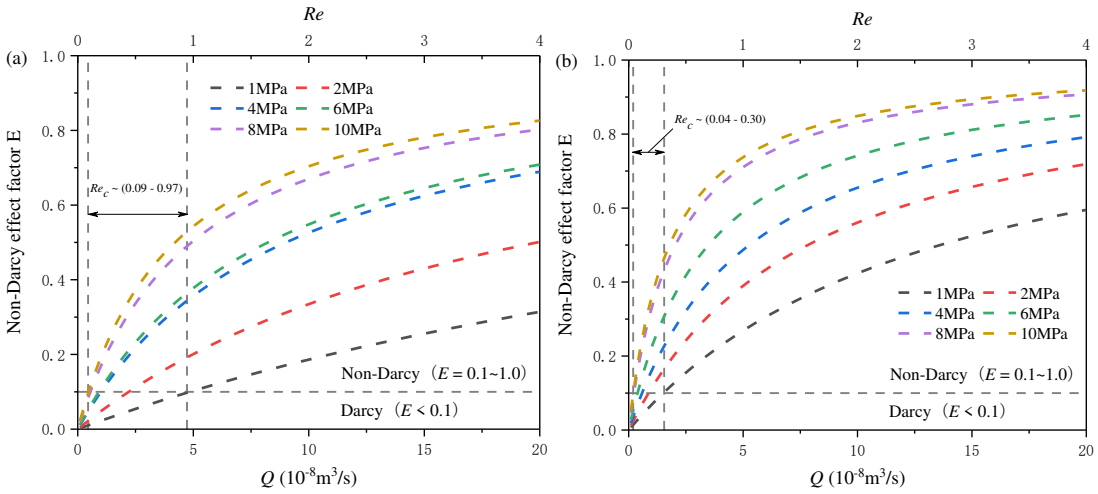

368

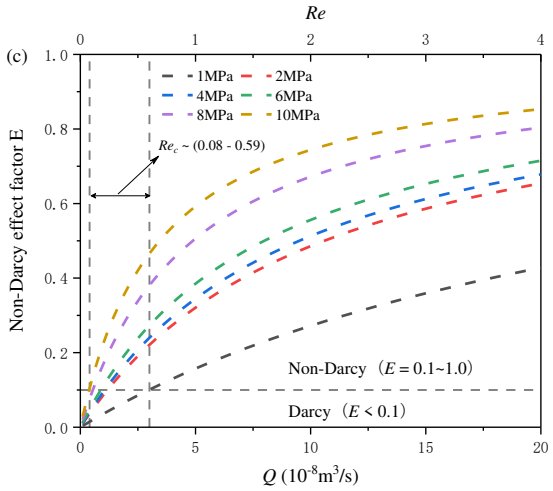

Fig. 11 Variation of non-Darcy effect factor E with Reynolds number Re and volume flow Q: (a)-(c) specimens S1-S3.

The collaborative influence of the contact and roughness of fractures on the critical Reynolds number Re_c didn't attract enough attention from many researchers. From the expression $B=\frac{\beta\rho}{w^2 e_h^2}$ (Eqs. (14)), the non-Darcy coefficient β can be determined by the geometry of the fracture. The nonlinear coefficient B and contact ratio c are fitted by an exponential function with a correlation coefficient greater than 0.986, shown in Fig. 12. Moreover, Louis (1969) proposed a logarithmic expression to describe the non-Darcy coefficient β related to the hydraulic aperture e_h and fracture peak asperity ξ as follows.

$$\beta=\frac{1}{8e_h}\left(\log f-\log\frac{\xi}{2e_h}\right) \quad (18)$$

where f is a dimensionless coefficient, determined by relative roughness $\frac{\xi}{2e_h}$.

Since the formula (18) didn't consider the influence of rough fracture contact on nonlinear seepage. A new formula (19) was derived based on the dimensional analysis and the power exponential function of the contact ratio and the nonlinear coefficient.

$$\beta=\frac{1}{e_h}(1+mc)^n\ln(pD_v) \quad (19)$$

where m, n, p are dimensionless coefficients, obtained by the fitting data. Substituting formula (19) into formula (14), the nonlinear coefficient B could be characterized by the contact ratio c and fractal dimension D_v of fracture.

$$B = \frac{\rho(1+mc)^n \ln(pD_v)}{w^2 e_h^3} \qquad (20)$$

Hence, corresponding curves about coefficients B, c and D_v are analyzed and shown in Fig. 13, presenting a good fitting correlation coefficient valued $R^2 = 0.932$, and the fitting coefficients m, n, p could be obtained as $m = 1.76, n = 16.54$, and $p = 0.72$ respectively. Comparing the predicted value of the nonlinear coefficient of formula (20) with the experimental value, as shown in Fig.14, the correlation coefficient is 0.979, which proves the effectiveness of the established nonlinear coefficient model.

So the critical Reynolds number Re_c can be written by the following Eq. (21) by substituting Eqs. (13) and (20) into Eq. (17).

$$Re_c = \frac{12E}{(1-E)(1+mc)^n \ln(pD_v)} \qquad (21)$$

The formula (21) provides a new method for predicting the Reynolds number Re_c by calculating the fractal dimension D_v and contact ratio c. As shown in Fig.15, the predicted critical Reynolds number Re_c is in good agreement with the experimental value under different contact ratios. Furthermore, the critical Reynolds number Re_c has a decreasing trend with increasing contact ratio, revealing the abrupt decline of effective flow channels and obvious tortuosity of the flow paths at a greater contact ratio.

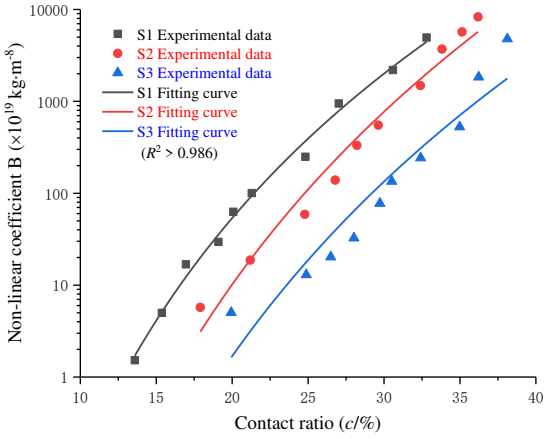

Fig. 12 Relationship curve between nonlinear coefficient B and contact ratio c.

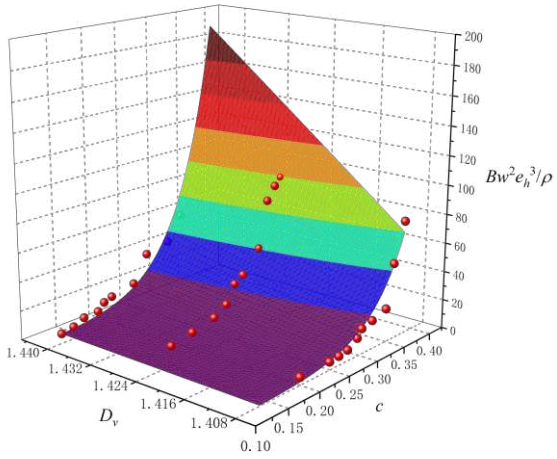

Fig. 13 Nonlinear coefficient B as a function of the contact ratio c and fractal dimension D_v.

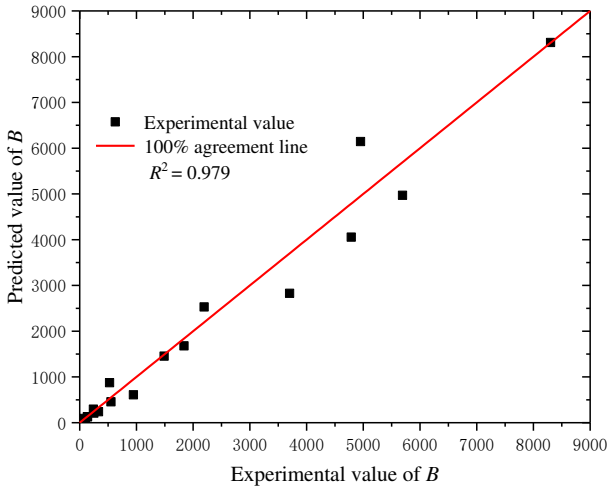

Fig.14 Comparison of the experimental and predicted values of the nonlinear coefficient B for S1-S3

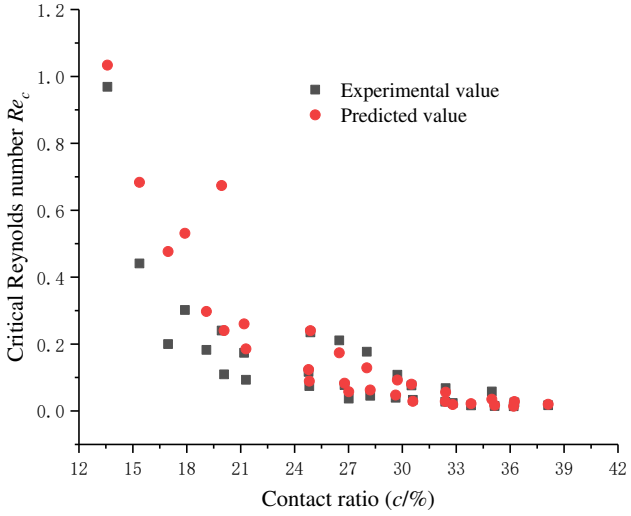

Fig. 15 Comparison of experimental data and the predicted value of the critical Reynolds number Re_c.

4 Numerical simulation

4.1 Governing equation

The seepage characteristics of fractured rock masses are usually characterized by the Navier-Stokes equation. However, due to the complexity and computational cost of the solution of the N-S equation, it is simplified into the Reynolds equation (Huang et al. 2017; Shen et al. 2020)， which can also better characterize the impact of contact on the seepage path.

$$\frac{\partial}{\partial x}\left(\frac{\rho g e_{ij}^{'3}}{12\mu}\frac{\partial h}{\partial x}\right)+\frac{\partial}{\partial y}\left(\frac{\rho g e_{ij}^{'3}}{12\mu}\frac{\partial h}{\partial y}\right)=0 \qquad (22)$$

where h is the water head of the fractures, $\Delta P=\rho g\Delta h$ is the water pressure, g is the gravitational acceleration, $e_{ij}^{'}$ represents the real-time aperture of different nodes in the aperture matrix under different normal stresses.

4.2 Verification of numerical simulations based on experiments

The rough fracture seepage is simulated by commercial software COMSOL Multiphysics, the PDE module is selected to set the Reynolds equation, the inlet and outlet of the fracture are set as pressure boundaries, and the side boundary is set as the wall with no flow, as shown in Fig.16. To verify the feasibility of the simulation, the flow rate through fracture can be analyzed by numerical integration, thus the equivalent permeability of the fracture is calculated according to the formula (23).

$$Q=A_s\frac{K}{\mu}\frac{\Delta P}{L} \qquad (23)$$

Where A_s is the cross-sectional area, K is the equivalent permeability. The simulated permeability and corresponding experimental values of the specimens S1, S2, and S3 subjected to normal stress are listed in Table 5. It can be observed that the relative error is less than 1% while comparing to the above-mentioned permeability, indicating that the verification of the simulation.

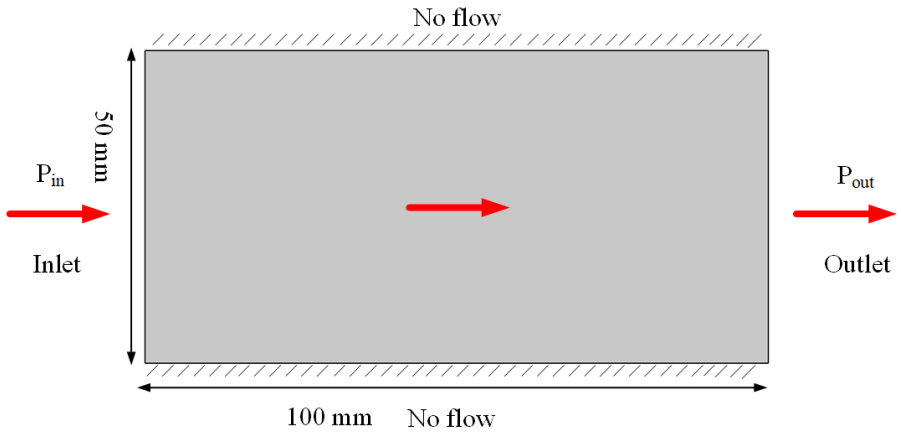

Fig.16 Boundary conditions of seepage

Table 5 Permeability of numerical and experimental results under different confining pressures

σ_n (MPa)	Permeability (10^{-11} m^2)						Relative error (%)		
	Experimental data			Simulation data					
	S1	S2	S3	S1	S2	S3	S1	S2	S3
1	9.114	8.176	10.396	9.134	8.102	10.292	0.226	0.899	0.999
2	6.961	5.373	5.609	7.018	5.346	5.566	0.812	0.488	0.775
4	5.247	3.257	4.478	5.275	3.277	4.466	0.529	0.612	0.266
6	3.832	2.420	3.670	3.864	2.421	3.645	0.838	0.046	0.664
8	3.265	1.937	2.854	3.245	1.921	2.846	0.623	0.824	0.292
10	2.655	1.513	2.495	2.673	1.515	2.520	0.656	0.122	1.000
15	1.682	0.989	1.816	1.673	0.984	1.824	0.538	0.530	0.472
20	1.102	0.757	1.207	1.104	0.753	1.219	0.147	0.466	0.977
25	0.675	0.609	0.907	0.669	0.611	0.911	0.855	0.288	0.431
30	0.492	0.490	0.629	0.490	0.486	0.629	0.470	0.900	0.052

4.3 Influence of contact ratio on seepage

The local contact of rough fractures subjected to normal stress can change effective flow channels and corresponding flow paths, resulting in the obvious transformation of seepage behavior. The experiments in section 3.1 have analyzed the normal closure displacement and contact ratio under different normal stresses, the detailed curves for specimens S1, S2, and S3 are plotted in Fig. 17. It is observed that the contact ratio of fracture enhances with increasing normal stress, otherwise, the permeability gradually decreases by two orders of magnitude. For better describing the influence of the contact on flow behavior through rough fractures, corresponding aperture distribution, and streamline distribution under different normal stresses are deeply investigated as follows.

The normal stress is zero in the initial state, and the fracture aperture distribution of specimens S1 under different normal stresses is shown in Fig. 18, where the white element represents the contact. The contact ratio could be calculated from the aperture distribution by formula (11). The contact ratio of specimen S1 under normal stress σ_n=1MPa , σ_n=10MPa , and σ_n=30MPa is respectively 13.59%, 21.29%, and 32.80%, increasing by 2.41 times, and the contact ratio of specimen S2 under normal stress σ_n=1MPa , σ_n=10MPa and σ_n=30MPa is respectively 17.90%, 29.63%, and 36.20%, increasing by 2.02 times, and the contact ratio of specimen S3 under confining pressure σ_n=1MPa , σ_n=10MPa and σ_n=30MPa is respectively 19.94%, 30.51%, and 38.12%, increasing by 1.91 times. It can be concluded from the aperture distribution and variation of the contact ratio that increasing normal stress expands the number of the local contact elements and a greater contact ratio. Overall, the rougher fracture, the greater the increase in contact ratio, and the less easily the fracture is compressed.

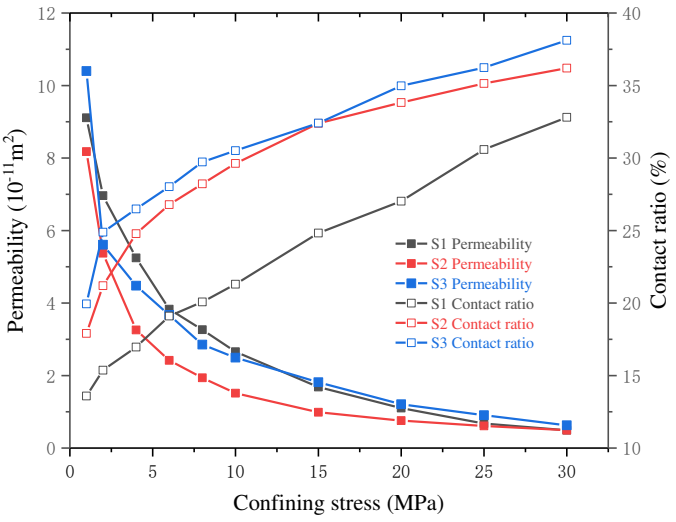

Fig.17 Relationship between permeability and contact ratio with normal stress

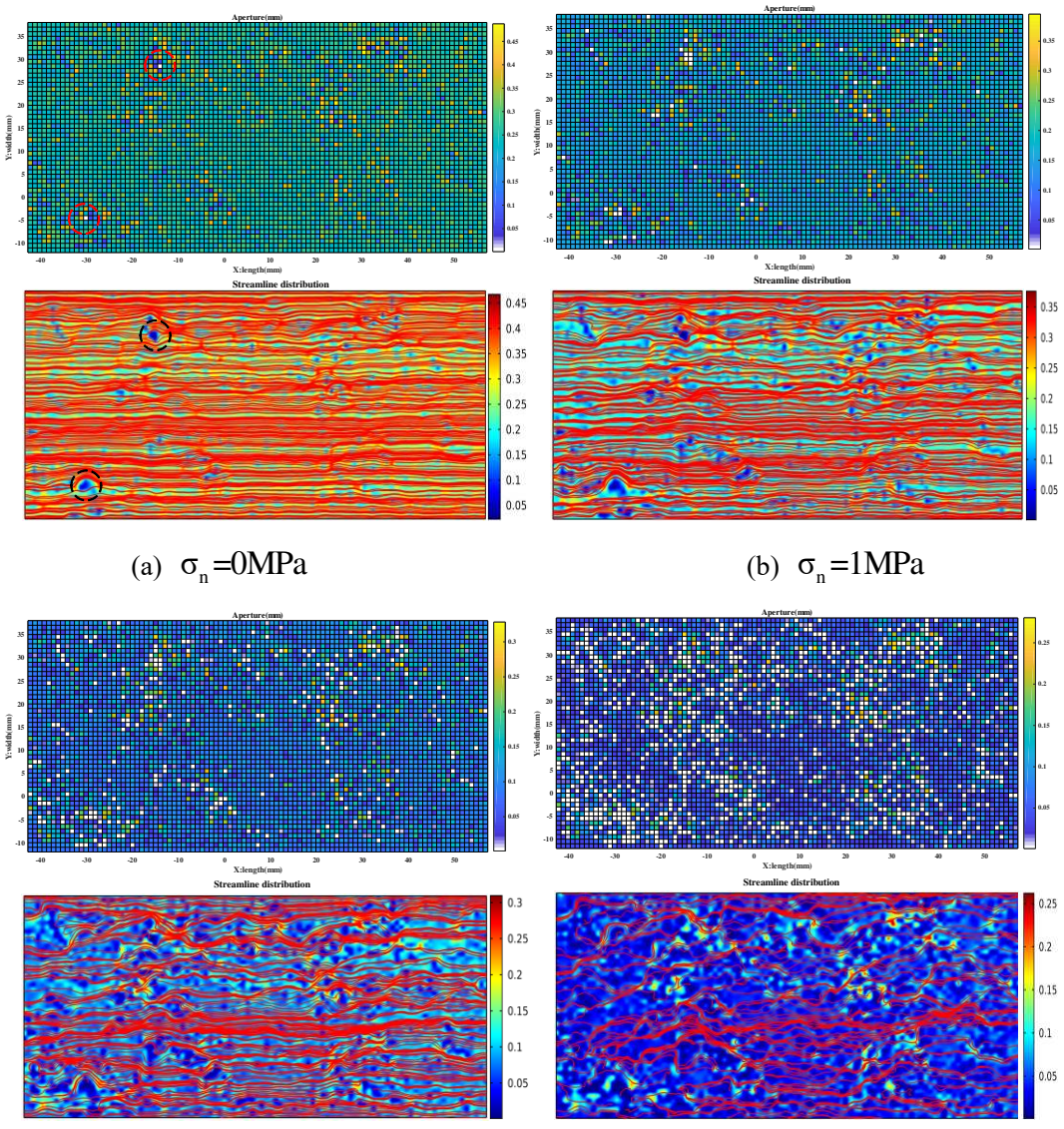

(a) σ_n=0MPa (b) σ_n=1MPa

(c) σ_n=10MPa (d) σ_n=30MPa

Fig.18 Distribution of aperture and streamline for S1 under different stresses (White denotes contact)

5 Conclusions

In this study, the seepage experiments of rough fractures under different confining pressures were conducted, and the effect of fractal dimension and contact in the fracture on flow behavior was deeply investigated. Besides, the experimental data were taken to verify the rationality of the proposed numerical model. The following conclusions are drawn:

(1) The flow behavior through rough fractures transforms from linearity to nonlinearity while increasing the hydraulic gradient. With the rise of normal stress, the seepage channel is compressed, and the contact between the upper and lower fracture

surfaces gradually increases, which intensifies the nonlinearity of seepage. Based on experimental data, it is verified that the Forchheimer equations can better characterize the nonlinear seepage flow in the rough fracture. Both the linear coefficient A and the nonlinear coefficient B increase with the rise of confining pressure.

(2) The relationship curve between normal displacement and normal stress is in good agreement with the Bandis model, and the maximum normal displacement value is obtained by fitting the curve. The ratios of the maximum normal displacement of fractures S1-S3 to the initial aperture are 96.25%, 96.73%, and 97.55%, which are slightly smaller than the initial aperture, and the fracture is rougher, the smaller $u_{\max}/e_m$ is. Besides, a modified Bandis model is proposed to calculate the normal displacement considering the fractal dimension of the fracture.

(3) The nonlinear coefficient B has a good power exponential relationship with the contact ratio C of the fracture, and a new model to describe the nonlinear coefficient B is developed depending on contact ratio C and fractal dimension D_v. Moreover, an empirical equation is derived to obtain the critical Reynolds number by combining the linear coefficients A with the non-Darcy effect factor E.

(4) As the confining pressure increased, the contact ratio of fracture gradually raises, however, the permeability decreases. Besides, due to the fewer contact elements, the seepage path of the fracture has only a small tortuosity near the contact elements under initial conditions. When the normal stress gradually raises, the effective channels of seepage decrease sharply attributed to the increase of the contact elements of the fracture, resulting in more tortuous flow paths.

Conflicts of Interest

The authors declare that there are no conflicts of interest regarding the publication of this paper.

Acknowledgments

The research is financially supported by the National Natural Science Foundation of China No.51779021 and the Fundamental Research Funds for the Central Universities No.2020CDCGJ021.

References

Babadagli T, Ren XJ, Develi K (2015) Effects of fractal surface roughness and lithology on single and multiphase flow in a single fracture: An experimental investigation International Journal of Multiphase Flow 68:40-58

Bandis SC, Lumsden AC, Barton NR (1983) Fundamentals of Rock Joint Deformation International Journal of Rock Mechanics and Mining Sciences 20:249-268

Brown SR (1987) Fluid-Flow through Rock Joints - the Effect of Surface-Roughness Journal of Geophysical Research-Solid Earth and Planets 92:1337-1347

Brush DJ, Thomson NR (2003) Fluid flow in synthetic rough-walled fractures: Navier-Stokes, Stokes, and local cubic law simulations Water Resources Research 39

Chen Y-F, Zhou J-Q, Hu S-H, Hu R, Zhou C-B (2015) Evaluation of Forchheimer equation coefficients for non-Darcy flow in deformable rough-walled fractures Journal of Hydrology 529:993-1006

Chen YD, Lian HJ, Liang WG, Yang JF, Nguyen VP, Bordas SPA (2019) The influence of fracture geometry variation on non-Darcy flow in fractures under confining stresses International Journal of Rock Mechanics and Mining Sciences 113:59-71

Chen YD, Liang WG, Lian HJ, Yang JF, Nguyen VP (2017) Experimental study on the effect of fracture geometric characteristics on the permeability in deformable rough-walled fractures International Journal of Rock Mechanics and Mining Sciences 98:121-140

Chen YF, Hu SH, Wei K, Hu R, Zhou CB, Jing LR (2014) Experimental characterization and micromechanical modeling of damage-induced permeability variation in Beishan granite International Journal of Rock Mechanics and Mining Sciences 71:64-76

Crandall D, Bromhal G, Karpyn ZT (2010) Numerical simulations examining the relationship between wall-roughness and fluid flow in rock fractures International Journal of Rock Mechanics and Mining Sciences 47:784-796

Ge YF, Kulatilake PHSW, Tang HM, Xiong CR (2014) Investigation of natural rock joint roughness Computers and Geotechnics 55:290-305

Greenwood JA, Williamson JB (1966) Contact of Nominally Flat Surfaces Proceedings of the Royal Society of London Series a-Mathematical and Physical Sciences 295:300-+

Huang N, Liu RC, Jiang YJ (2017) Numerical study of the geometrical and hydraulic characteristics of 3D self-affine rough fractures during shear Journal of Natural Gas Science and Engineering 45:127-142

Javadi M, Sharifzadeh M, Shahriar K (2010) A new geometrical model for non-linear fluid flow through rough fractures Journal of Hydrology 389:18-30

Javadi M, Sharifzadeh M, Shahriar K, Mitani Y (2014) Critical Reynolds number for nonlinear flow through rough-walled fractures: The role of shear processes Water Resources Research 50:1789-1804

Kulatilake PHSW, Park J, Balasingam P, Morgan R (2007) Quantification of Aperture and Relations Between Aperture, Normal Stress and Fluid Flow for Natural Single Rock Fractures Geotechnical and Geological Engineering 26:269-281

Li B, Jiang YJ, Koyama T, Jing LR, Tanabashi Y (2008) Experimental study of the hydro-mechanical behavior of rock joints using a parallel-plate model containing contact areas and artificial fractures International Journal of Rock Mechanics and Mining Sciences 45:362-375

Li B, Zhao ZH, Jiang YJ, Jing LR (2015) Contact mechanism of a rock fracture subjected to normal loading and its impact on fast closure behavior during initial stage of fluid flow experiment International Journal for Numerical and Analytical Methods in Geomechanics 39:1431-1449

Liu RC, Huang N, Jiang YJ, Jing HW, Yu LY (2020a) A numerical study of shear-induced evolutions of geometric and hydraulic properties of self-affine rough-walled rock fractures International Journal of Rock Mechanics and Mining Sciences 127

Liu RC, Li B, Jiang YJ (2016) Critical hydraulic gradient for nonlinear flow through rock fracture networks: The roles of aperture, surface roughness, and number of intersections Advances in Water Resources 88:53-65

Liu X, Li M, Zeng N, Li T (2020b) Investigation on Nonlinear Flow Behavior through Rock Rough Fractures Based on Experiments and Proposed 3-Dimensional Numerical Simulation Geofluids 2020:1-34

Liu XS, Li M, Xu M, Kang ZY (2020c) Permeability of the Hydrated Shale under Cyclic Loading and Unloading Conditions Geofluids 2020:1-16

Louis C (1969) A Study of groundwater flow in jointed rock and its influence on stability of rock mass Imperial College Rock Mechanics Report 10

Pyraknolte LJ, Morris JP (2000) Single fractures under normal stress: The relation between fracture specific stiffness and fluid flow International Journal of Rock Mechanics and Mining Sciences 37:245-262

Radilla G, Nowamooz A, Fourar M (2013) Modeling Non-Darcian Single- and Two-Phase Flow in Transparent Replicas of Rough-Walled Rock Fractures Transport in Porous Media 98:401-426

Ranjith PG, Darlington W (2007) Nonlinear single-phase flow in real rock joints Water Resources Research 43

Rong G, Yang J, Cheng L, Zhou CB (2016) Laboratory investigation of nonlinear flow characteristics in rough fractures during shear process Journal of Hydrology 541:1385-1394

Rutqvist J (2015) Fractured rock stress-permeability relationships from in situ data and effects of temperature and chemical-mechanical couplings Geofluids 15:48-66

Shen ZH, Zhou L, Li HL, Lu ZH, Cai JC (2020) Experimental and Numerical Study on the Anisotropic and Nonlinear Gas Flow Behavior of a Single Coal Fracture under Loading Energy & Fuels 34:4230-4242

Song F, Bo L, Zhang S, Sun Y (2019) Nonlinear flow in low permeability reservoirs: Modelling and experimental verification Advances in Geo-Energy Research 3:76-81

Tse R, Cruden DM (1979) Estimating Joint Roughness Coefficients International Journal of Rock Mechanics and Mining Sciences 16:303-307

Wang L, Cardenas MB, Slottke DT, Ketcham RA, Sharp JM (2015) Modification of the Local Cubic Law of fracture flow for weak inertia, tortuosity, and roughness Water Resources Research 51:2064-2080

Wang M, Chen YF, Ma GW, Zhou JQ, Zhou CB (2016) Influence of surface roughness on nonlinear flow behaviors in 3D self-affine rough fractures: Lattice Boltzmann simulations Advances in Water Resources 96:373-388

Wanniarachchi WAM, Ranjith PG, Perera MSA, Rathnaweera TD, Zhang C, Zhang DC (2018) An integrated approach to simulate fracture permeability and flow characteristics using regenerated rock fracture from 3-D scanning: A numerical study Journal of Natural Gas Science and Engineering 53:249-262

Xia CC, Qian X, Lin P, Xiao WM, Gui Y (2017) Experimental Investigation of Nonlinear Flow Characteristics of Real Rock Joints under Different Contact Conditions Journal of Hydraulic Engineering 143

Xiong F, Jiang QH, Chen MX (2018a) Numerical Investigation on Hydraulic Properties of Artificial-Splitting Granite Fractures during Normal and Shear Deformations Geofluids 2018:1-16

Xiong F, Jiang QH, Ye ZY, Zhang XB (2018b) Nonlinear flow behavior through rough-walled rock fractures: The effect of contact area Computers and Geotechnics 102:179-195

Yang J, Rong G, Hou D, Peng J, Zhou C (2015) Experimental Study on Peak Shear Strength Criterion for Rock Joints Rock Mechanics and Rock Engineering 49:821-835

Yao C, Shao Y, Yang J, Huang F, He C, Jiang Q, Zhou C (2020) Effects of non-darcy flow on heat-flow coupling process in complex fractured rock masses Journal of Natural Gas Science and Engineering 83

Yeo W (2001) Effect of contact obstacles on fluid flow in rock fractures Geosciences Journal 5:139-143

Yu J, Yao W, Duan K, Liu X, Zhu Y (2020) Experimental study and discrete element method modeling of compression and permeability behaviors of weakly anisotropic sandstones International Journal of Rock Mechanics and Mining Sciences 134

Zeng ZW, Grigg R (2006) A criterion for non-Darcy flow in porous media Transport in Porous Media 63:57-69

Zhang G, Zhang Y, Xu A, Li Y (2019) Microflow effects on the hydraulic aperture of single rough fractures Advances in Geo-Energy Research 3:104-114

Zhang ZY, Nemcik J (2013) Fluid flow regimes and nonlinear flow characteristics in deformable rock fractures Journal of Hydrology 477:139-151

Zhao Y, Wang CL, Bi J (2020) Analysis of Fractured Rock Permeability Evolution Under Unloading Conditions by the Model of Elastoplastic Contact Between Rough Surfaces Rock Mechanics and Rock Engineering

Zhou JQ, Hu SH, Chen YF, Wang M, Zhou CB (2016) The Friction Factor in the Forchheimer Equation for Rock Fractures Rock Mechanics and Rock Engineering 49:3055-3068

Zhou JQ, Hu SH, Fang S, Chen YF, Zhou CB (2015) Nonlinear flow behavior at low Reynolds numbers through rough-walled fractures subjected to normal compressive loading International Journal of Rock Mechanics and Mining Sciences 80:202-218 doi:10.1016/j.ijrmms.2015.09.027

Zimmerman RW, Al-Yaarubi A, Pain CC, Grattoni CA (2004) Non-linear regimes of fluid flow in rock fractures International Journal of Rock Mechanics and Mining Sciences 41:384-384

Zimmerman RW, Yeo I-W Fluid flow in rock fractures: From the navier-stokes equations to the cubic law. In, 2000 2000. vol Conference Proceedings. pp 213-224

Zou L, Li B, Mo Y, Cvetkovic V (2019) A High-Resolution Contact Analysis of Rough-Walled Crystalline Rock Fractures Subject to Normal Stress Rock Mechanics and Rock Engineering 53:2141-2155

Zou LC, Jing LR, Cvetkovic V (2017) Shear-enhanced nonlinear flow in rough-walled rock fractures International Journal of Rock Mechanics and Mining Sciences 97:33-45

Figures

(a) Sampling location: Jiulongpo

(b) Sandstones specimens

Figure 1

Specimens of sandstone. Note: The designations employed and the presentation of the material on this map do not imply the expression of any opinion whatsoever on the part of Research Square concerning the legal status of any country, territory, city or area or of its authorities, or concerning the delimitation of its frontiers or boundaries. This map has been provided by the authors.

(a)Brazilian test

(b) Fracture surface after the Brazilian testing

Figure 2

Brazilian testing. Sandstone rough fracture preparation

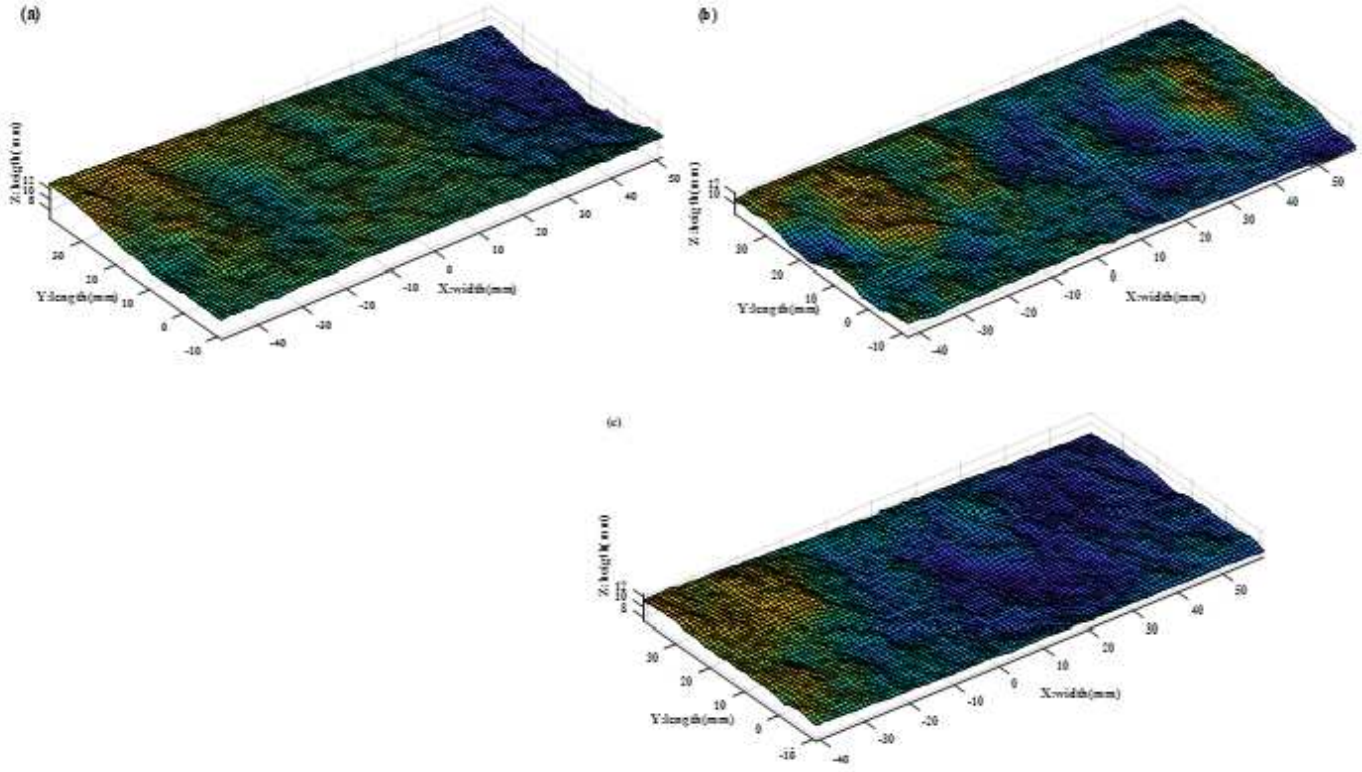

Figure 3

3-Dimensional morphology reconstruction of rough fracture of specimens:(a)-(c) specimens

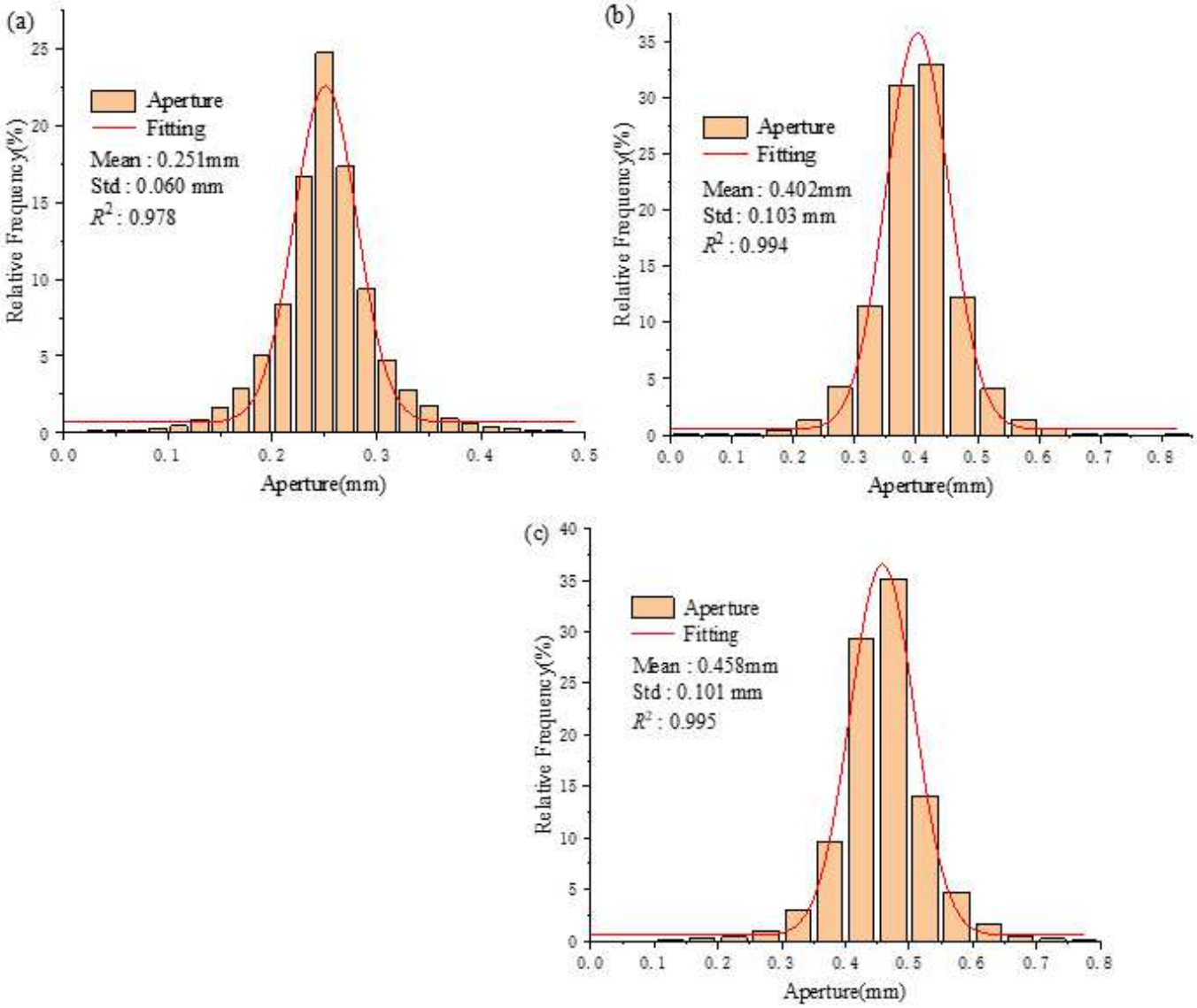

Figure 4

Aperture distribution of rough fracture surface : (a)-(c) specimens S1-S3

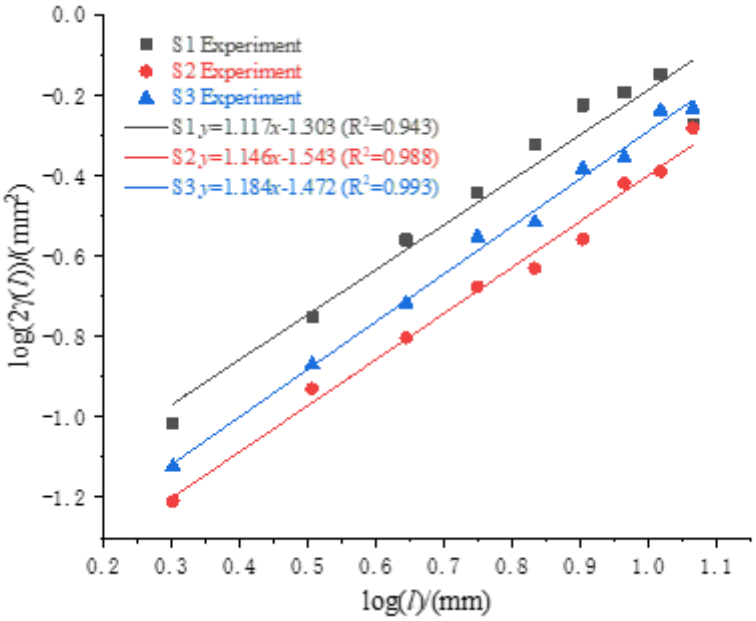

Figure 5

Please see the Manuscript PDF file for the complete figure caption.

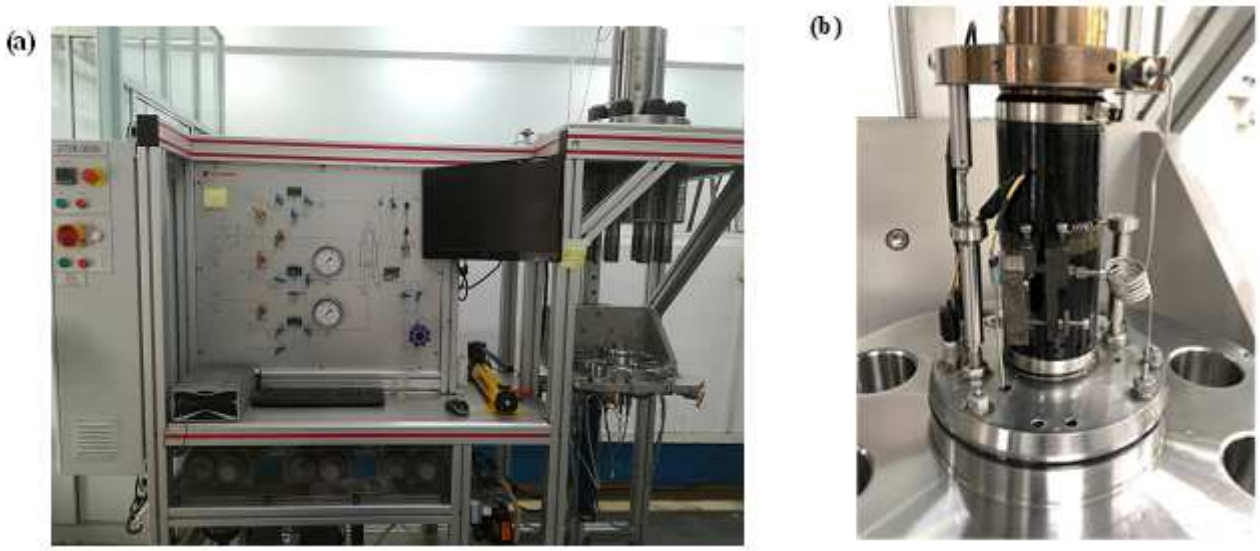

Figure 6

Triaxial multi-field coupling test system

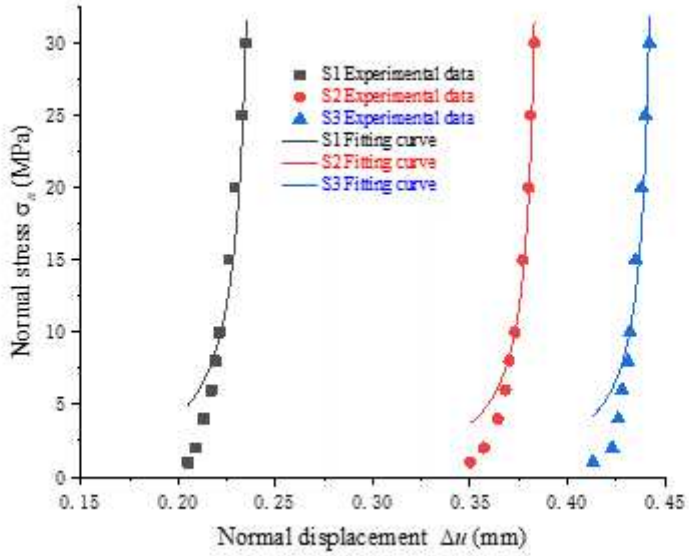

Figure 7

Relationship curve between normal stress and normal displacement

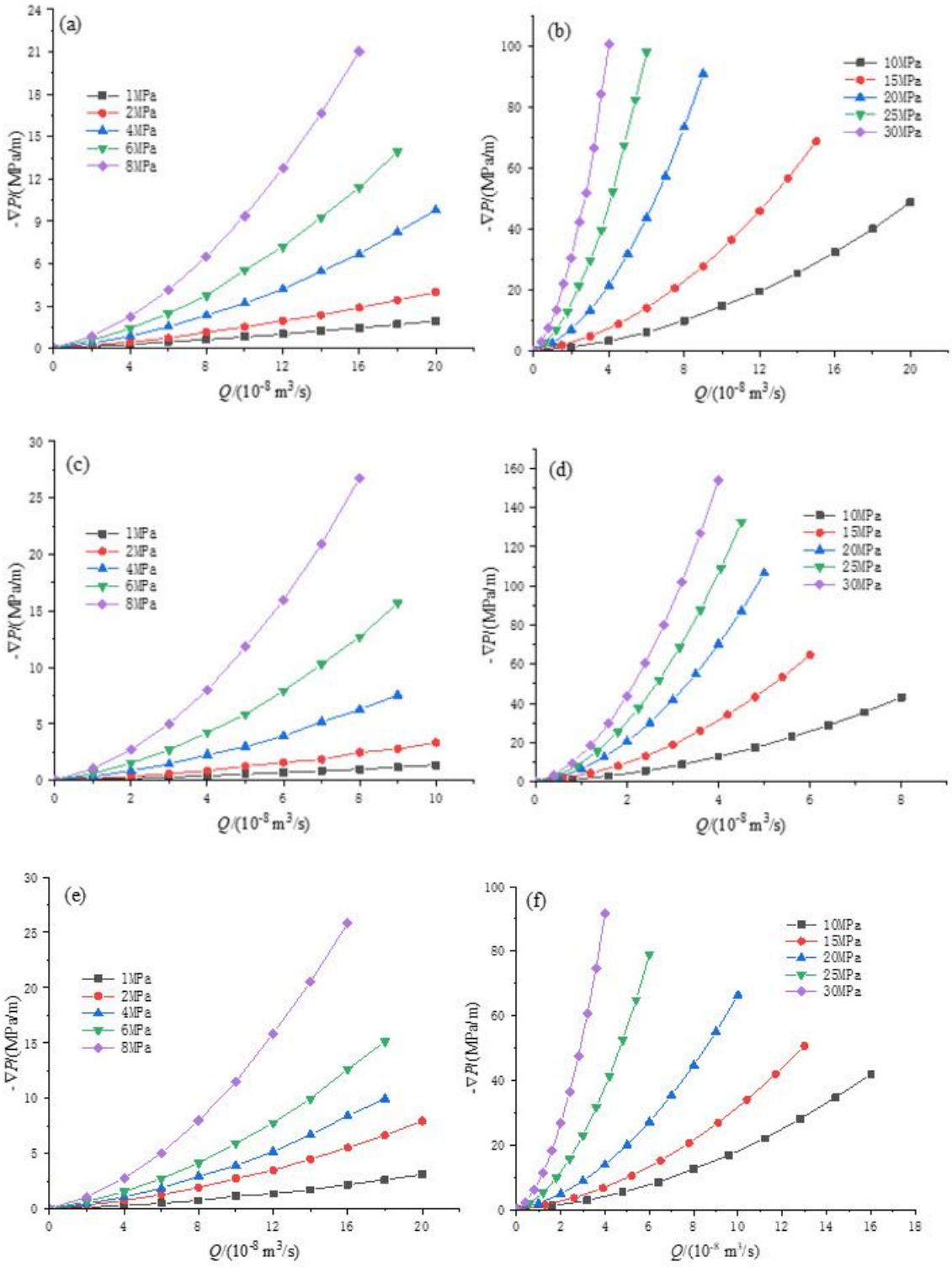

Figure 8

Please see the Manuscript PDF file for the complete figure caption.

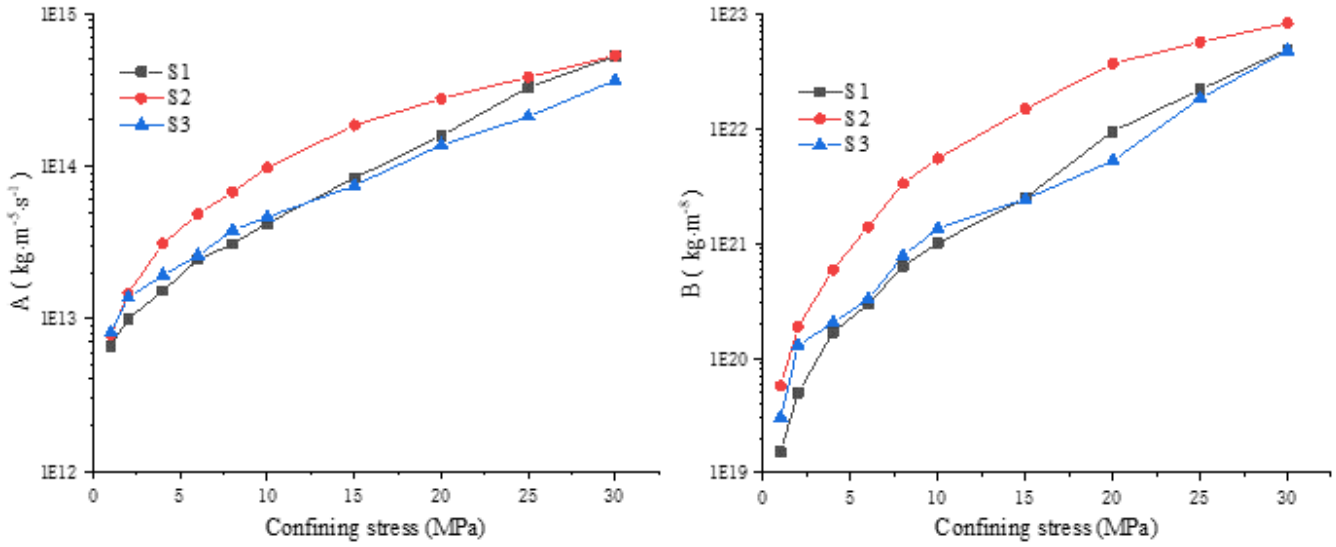

Figure 9

Relationship curve Forchheimer equation coefficients and confining pressure for S1-S3:(a) Coefficient A, Coefficient B

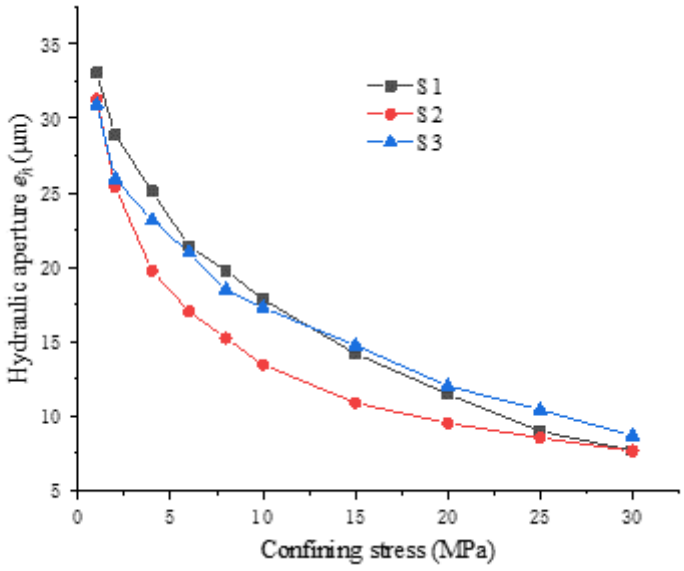

Figure 10

Variation of the hydraulic aperture with confining stress

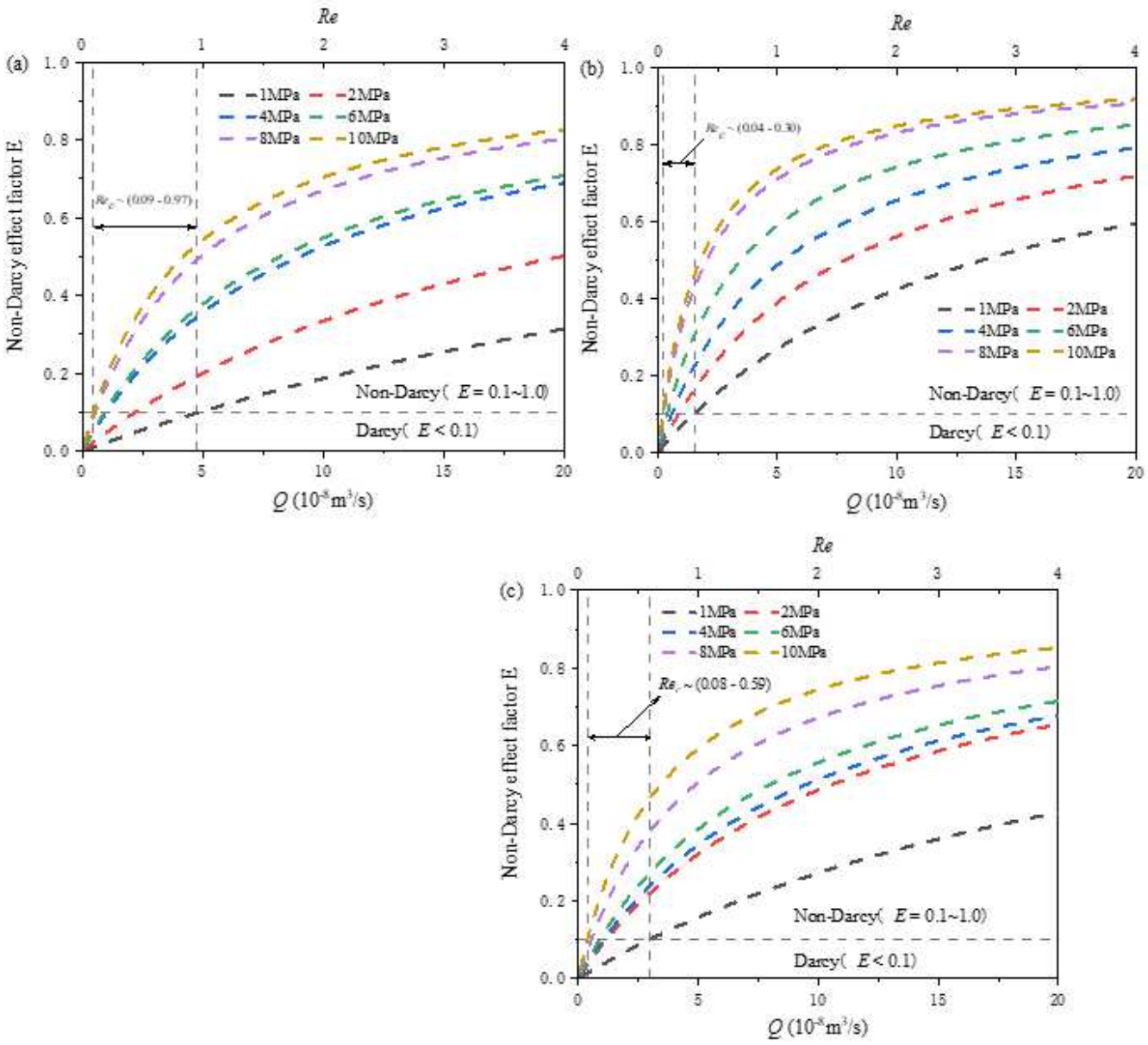

Figure 11

Variation of non-Darcy effect factor E with Reynolds number Re and volume flow Q : (a)-(c) specimens S1-S3.

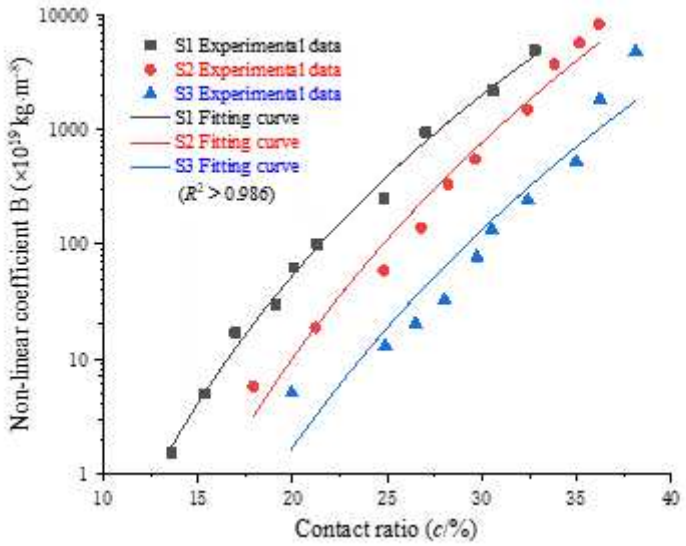

Figure 12

Relationship curve between nonlinear coefficient B and contact ratio c .

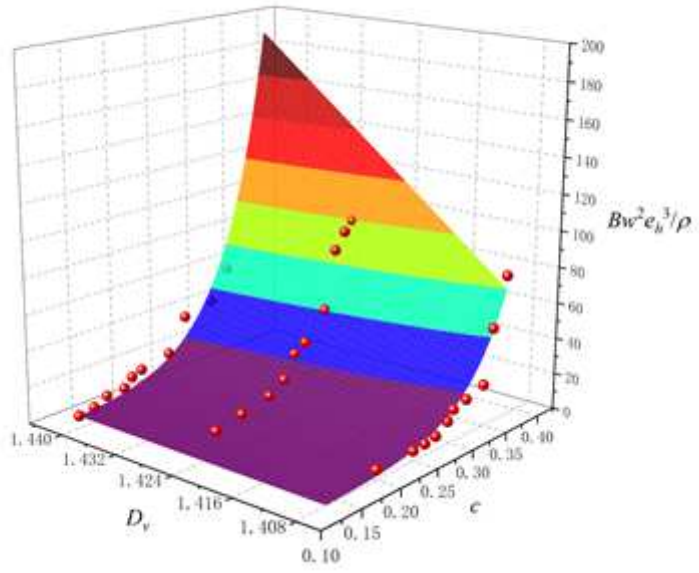

Figure 13

Nonlinear coefficient B as a function of the contact ratio c and fractal dimension Dv .

Figure 14

Comparison of the experimental and predicted values of the nonlinear coefficient B for S1-S3

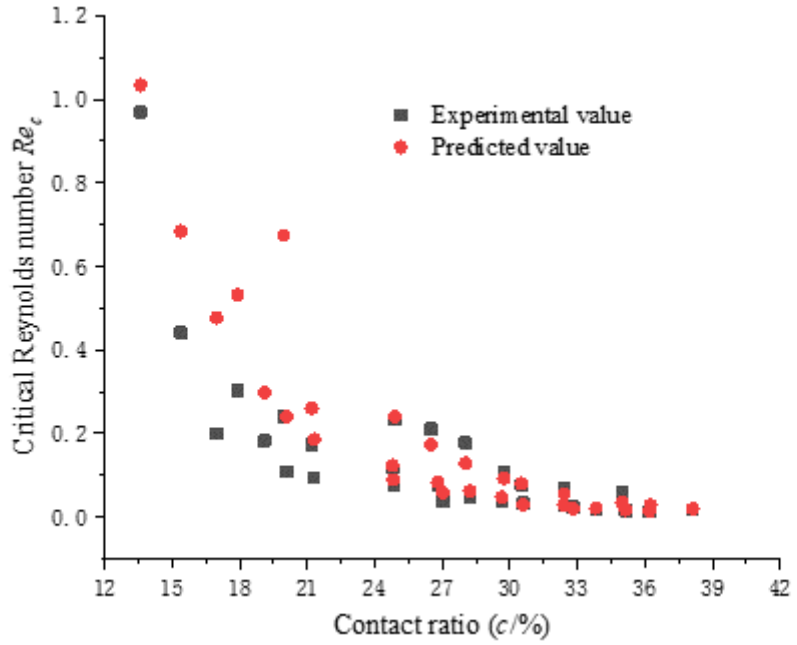

Figure 15

Comparison of experimental data and the predicted value of the critical Reynolds number Rec .

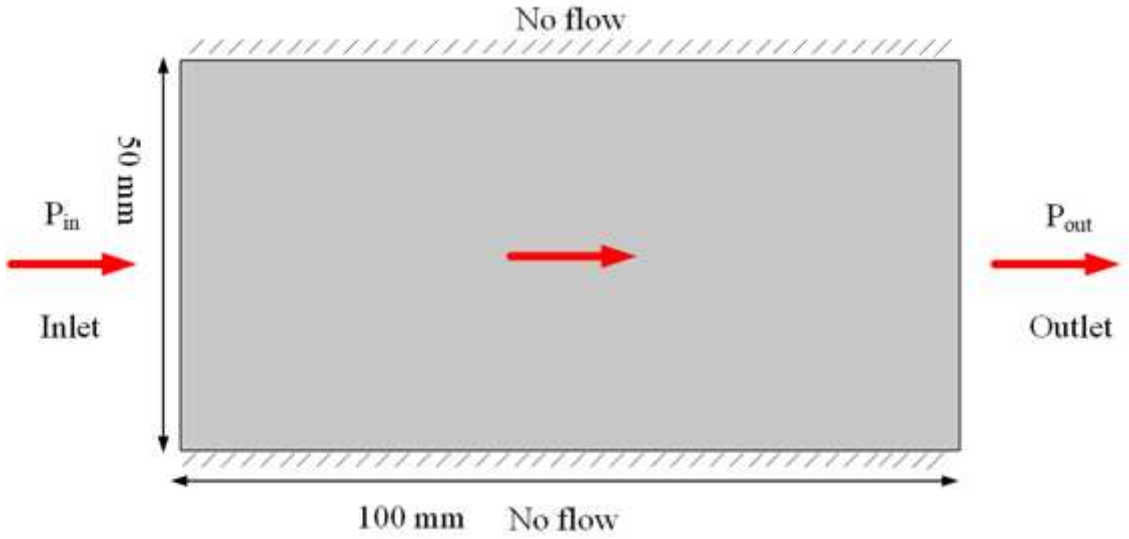

Figure 16

Boundary conditions of seepage

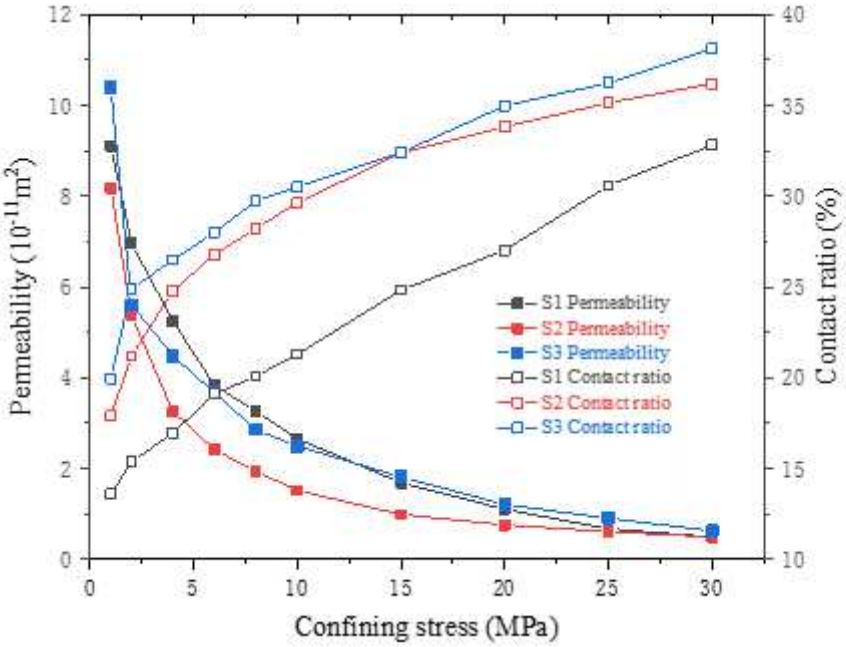

Figure 17

Relationship between permeability and contact ratio with normal stress

Figure 18

Distribution of aperture and streamline for S1 under different stresses (White denotes contact)